



## Multi-temporal MODIS–Landsat data fusion for relative radiometric normalization, gap filling, and prediction of Landsat data

David P. Roy <sup>a,\*</sup>, Junchang Ju <sup>a</sup>, Philip Lewis <sup>b</sup>, Crystal Schaaf <sup>c</sup>, Feng Gao <sup>d,e</sup>, Matt Hansen <sup>a</sup>, Erik Lindquist <sup>a</sup>

<sup>a</sup> Geographic Information Science Center of Excellence, South Dakota State University, Brookings, SD 57007, USA

<sup>b</sup> NERC Centre for Terrestrial Carbon Dynamics and Department of Geography, University College London, Gower Street, London, WC1E 6BT, UK

<sup>c</sup> Department of Geography and Environment, Boston University, Boston, MA 02215, USA

<sup>d</sup> Earth Resources Technology, Inc., 10810 Guilford Road, Annapolis Junction, MD 20701, USA

<sup>e</sup> NASA Goddard Space Flight Center, Code 614.4, USA

### ARTICLE INFO

#### Article history:

Received 5 October 2007

Received in revised form 6 March 2008

Accepted 8 March 2008

#### Keywords:

ETM+

MODIS

Data fusion

Radiometric normalization

BRDF

SLC-off gap filling

Image mosaicking

### ABSTRACT

A semi-physical fusion approach that uses the MODIS BRDF/Albedo land surface characterization product and Landsat ETM+ data to predict ETM+ reflectance on the same, an antecedent, or subsequent date is presented. The method may be used for ETM+ cloud/cloud shadow and SLC-off gap filling and for relative radiometric normalization. It is demonstrated over three study sites, one in Africa and two in the U.S. (Oregon and Idaho) that were selected to encompass a range of land cover/land use types and temporal variations in solar illumination, land cover, land use, and phenology. Specifically, the 30 m ETM+ spectral reflectance is predicted for a desired date as the product of observed ETM+ reflectance and the ratio of the 500 m surface reflectance modeled using the MODIS BRDF spectral model parameters and the sun-sensor geometry on the predicted and observed Landsat dates. The difference between the predicted and observed ETM+ reflectance (prediction residual) is compared with the difference between the ETM+ reflectance observed on the two dates (temporal residual) and with respect to the MODIS BRDF model parameter quality. For all three scenes, and all but the shortest wavelength band, the mean prediction residual is smaller than the mean temporal residual, by up to a factor of three. The accuracy is typically higher at ETM+ pixel locations where the MODIS BRDF model parameters are derived using the best quality inversions. The method is most accurate for the ETM+ near-infrared (NIR) band; mean NIR prediction residuals are 9%, 12% and 14% of the mean NIR scene reflectance of the African, Oregon and Idaho sites respectively. The developed fusion approach may be applied to any high spatial resolution satellite data, does not require any tuning parameters and so may be automated, is applied on a per-pixel basis and is unaffected by the presence of missing or contaminated neighboring Landsat pixels, accommodates for temporal variations due to surface changes (e.g., phenological, land cover/land use variations) observable at the 500 m MODIS BRDF/Albedo product resolution, and allows for future improvements through BRDF model refinement and error assessment.

© 2008 Elsevier Inc. All rights reserved.

### 1. Introduction

The Landsat satellite series represents the longest temporal record of space-based earth observations (Williams et al., 2006). The current Landsat systems, carrying the Landsat Thematic Mapper (Landsat 5) and the Enhanced Thematic Mapper Plus (ETM+) (Landsat 7), capture high spatial resolution scenes over a 183 km × 170 km extent with a 16-day revisit capability to provide a balance between requirements for localized high spatial resolution studies and large area monitoring (Arvidson et al., 2001; Goward et al., 2001). The primary limitation to the utility of Landsat data, other than data cost, is the availability of cloud-free surface observations; ETM+ land scenes are globally on average about 35% cloud covered (Ju & Roy, 2008), and in May 2003

the ETM+ scan line corrector (SLC) failed, reducing the usable data in each SLC-off scene by about 22% (Maxwell et al., 2007; Storey et al., 2005). As currently only the SLC-off Landsat ETM+ and the aging Landsat-5 TM (Chander et al., 2007; Helder & Ruggles, 2004) systems are acquiring data, and only a single successor Landsat Data Continuity

**Table 1**

Landsat ETM+ bands and the corresponding MODIS bands used in this study

Landsat ETM+ band wavelength (μm); band number in parentheses	MODIS band wavelength (μm); band number in parentheses
0.45–0.52 (1)	0.459–0.479 (3)
0.53–0.61 (2)	0.545–0.565 (4)
0.63–0.69 (3)	0.620–0.670 (1)
0.78–0.90 (4)	0.841–0.876 (2)
1.55–1.75 (5)	1.628–1.654 (6)
2.09–2.35 (7)	2.105–2.155 (7)

\* Corresponding author.

E-mail address: [david.roy@sdstate.edu](mailto:david.roy@sdstate.edu) (D.P. Roy).

**Table 2**  
Landsat ETM+ acquisitions for the three study sites (Fig. 1)

Site location	Path/row	Scene center latitude, longitude	Acquisition date	Mean solar zenith, solar azimuth	Cloud %
Africa (Congo/Sudan/Uganda)	P173R058	2.89°, 30.25°	2001/01/09	39.0°, 131.3°	0%
			2001/11/25	34.9°, 133.9°	6%
U.S. Idaho	P042R028	46.03°, -116.25°	2000/07/11	29.9°, 137.6°	0%
			2000/09/13	45.9°, 152.1°	0%
U.S. Oregon	P043R029	44.61°, -118.34°	2000/06/16	27.3°, 134.0°	0%
			2000/10/06	52.7°, 156.9°	0%

Landsat cloud fraction percentage data are obtained from USGS Global Visualization Viewer and generally underestimate the cloud cover observed in all scenes by ~5%.

**Table 3**

MODIS 16-day 500 m BRDF/Albedo product (MCD43A1 and MCD43A2) instances for the three study sites

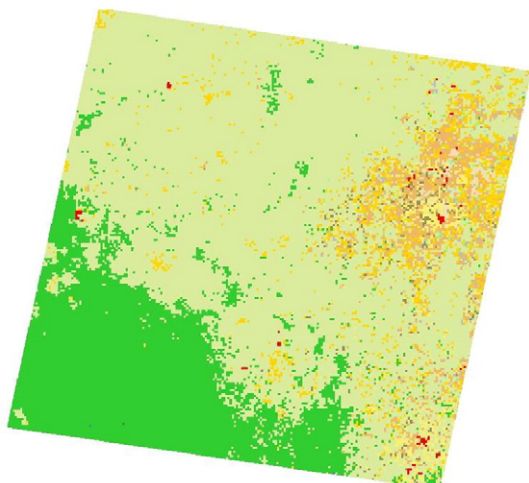
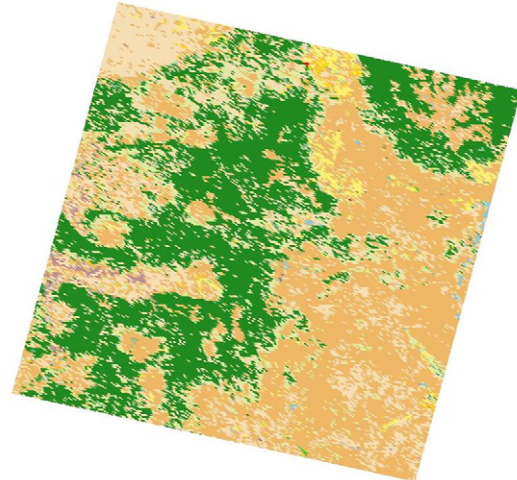
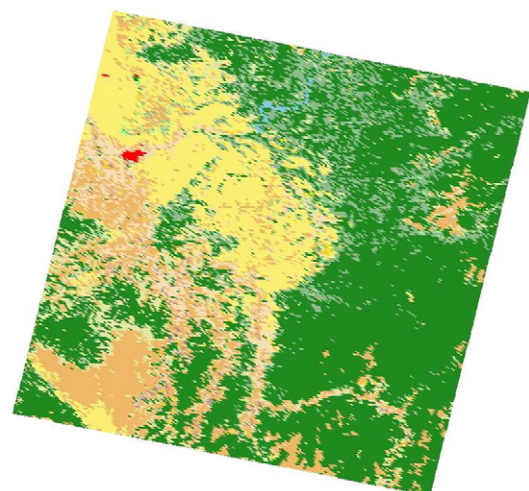
Site location	MODIS Tile ID	MCD43 date ranges	Mean NDVI
Africa Congo/Sudan/Uganda	h20v08, h21v08	2001, 01/01 to 01/16	0.59
		2001, 11/17 to 12/02	0.75
U.S. Idaho	h09v04, h10v04	2000, 07/03 to 07/18	0.66
		2000, 09/05 to 09/20	0.55
U.S. Oregon	h09v04	2000, 06/09 to 06/24	0.50
		2000, 09/29 to 10/14	0.41

The MODIS Tile ID shows the horizontal (h) and vertical (v) tile coordinates. The date ranges indicate the 16-day periods used to generate the products. The mean NDVI is calculated from nadir BRDF-adjusted red and near-infrared band surface reflectance for all cloud-free MODIS pixels encompassing the corresponding study sites (Fig. 1).

Mission (LDCM) sensor is scheduled for launch early in the next decade (Irons & Masek, 2006), a potential solution to provide more frequent high resolution surface observations is to fuse Landsat observations with data from other remote sensing systems. Landsat fusion is not straightforward however because the radiometric consistency of Landsat data may change spatially and temporally, due to atmospheric and phenological variations, differences in illumination and observation angles, cloud and shadow contamination, and sensor calibration changes (Coppin et al., 2004; Song & Woodcock, 2003). Methods to radiometrically normalize Landsat data have used relative approaches, which rely on the identification of pseudo-invariant features in spatially overlapping acquisitions and the application of statistical calibration relationships (Olthof et al., 2005; Schott et al., 1988), or absolute approaches based on the application of engineering calibration coefficients typically followed by atmospheric correction (Liang et al., 2001). In this paper a method for fusion of multi-temporal Landsat and Moderate Resolution Imaging Spectroradiometer (MODIS) is presented that provides a relative normalization and the ability to predict Landsat ETM+ reflectance.

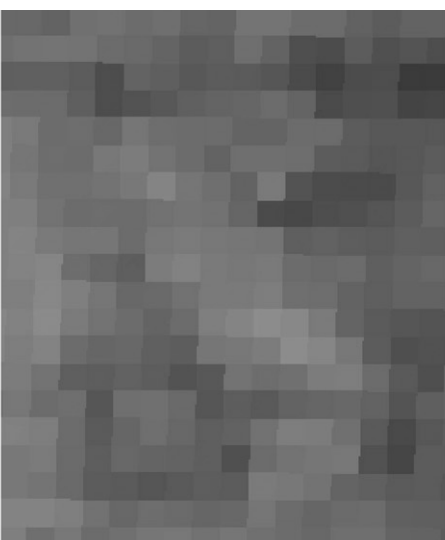
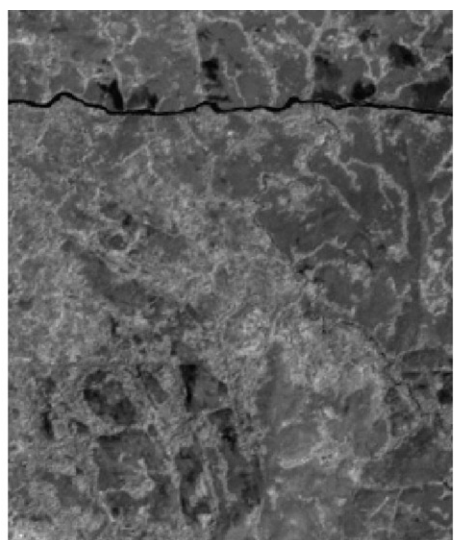
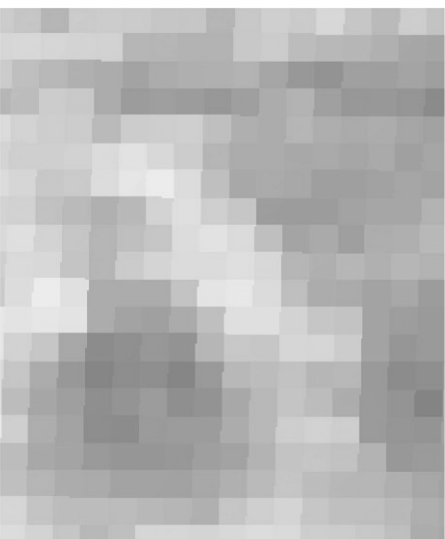
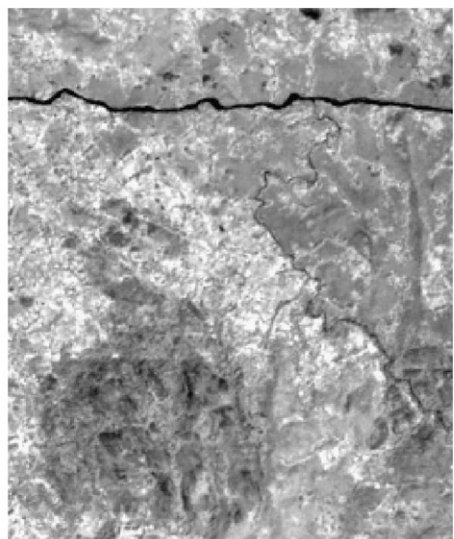
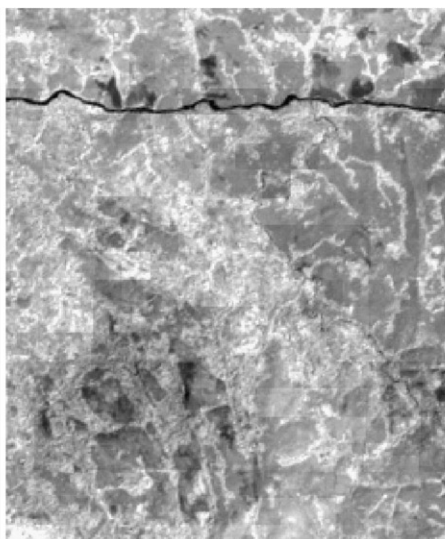
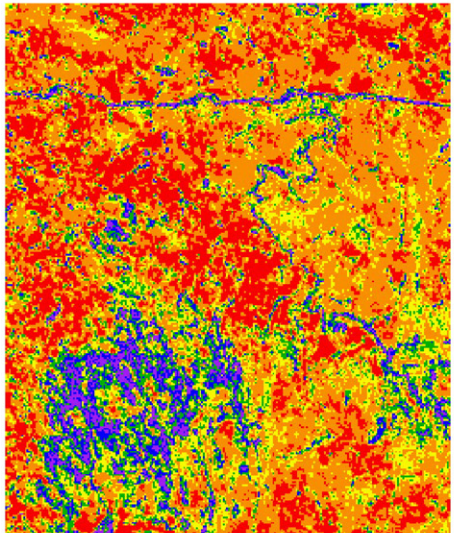
Fusion of remotely sensed data sensed from different satellite systems allows for exploitation of their different spectral, spatial, angular (viewing and solar geometry), and temporal sensing char-

acteristics (Pohl & Van Genderen, 1998). Satellite data fusion typically provides more observations of the surface within a given period, increasing the availability of cloud-free data in regions with a diurnal variability of cloud (Roy et al., 2006) and potentially provides more observations for inversion of physically-based models (Lucht & Lewis, 2000). Optical wavelength data fusion can be undertaken in an

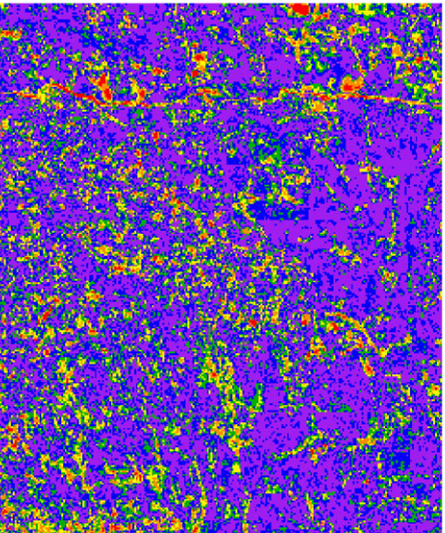
**a. Africa****b. Oregon****c. Idaho**

**Fig. 1.** The MODIS 1 km land cover product (2001) showing the three test scenes: (a) Africa, (b) U.S. Oregon, and (c) U.S. Idaho. Land cover classes (International Geosphere Biosphere Programme scheme) are color coded as:

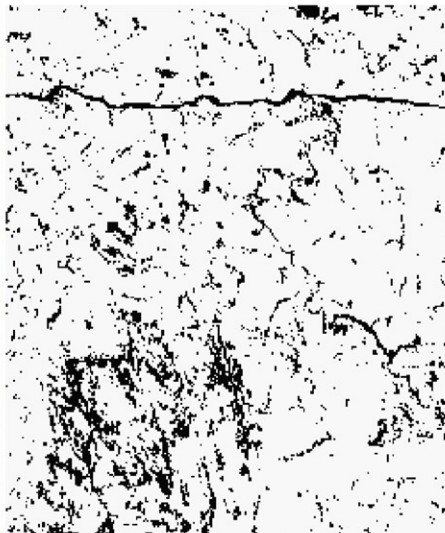
water,	evergreen needle-leaf forest	evergreen broadleaf forest
deciduous needle-leaf forest	deciduous broadleaf forest	mixed forest
closed shrublands	open shrublands	open shrublands
savanna,	grasslands	wetlands
croplands	built-up	crop/vegetation mosaic
white is snow/ice	barren	barren

a. Observed 2001/01/09 ETM+ NIR TOA  $\rho$ b. Modeled MODIS 2001/01/09 NIR surface  $\rho$ c. Observed 2001/11/25 ETM+ NIR TOA  $\rho$ d. Modeled MODIS 2001/11/25 NIR surface  $\rho$ e. Predicted 2001/11/25 ETM+ NIR TOA  $\rho$ 

f. Temporal residual



g. Prediction residual



h. Black means g is higher than f

empirical manner, for example, by extraction and compositing of spectral vegetation indices derived from different systems (van Leeuwen et al., 2006), weighting reflectances from different sensors according to their spectral differences (Gao et al., 2006; Olthof et al., 2005), or using more physically-based approaches, for example by inversion of Bi-directional Reflectance Distribution Function (BRDF) models (d'Entremont et al., 1999; Jin et al., 2002) or using data assimilation techniques (Quaife et al., 2008). Reliable fusion requires that the data from each system are precisely co-registered, calibrated, spectrally normalized to common wavebands, and atmospherically corrected using appropriate atmospheric characterization information, although the requirement for common wavebands can potentially be relaxed if physically-based reflectance models are used in merging data (Pinty et al., 2004). The fusion of data at different spatial resolutions is common, a typical example being 'pan sharpening' where the aim is to simulate a higher spatial resolution multispectral dataset from co-registered high resolution panchromatic and lower resolution multispectral data (Pohl & Van Genderen, 1998).

The current Landsat systems have a narrow 15° field of view, sensing high spatial resolution data with a 16-day revisit capability. This is in contrast to the 110° field of view, moderate spatial resolution, near daily global observations sensed by MODIS (Wolfe et al., 1998). These systems are in the same polar orbit, with Landsat ETM+ observations occurring approximately 15 min before MODIS Terra nadir observations. Recognizing the complementary aspects of these systems, Gao et al. (2006) developed an empirical fusion technique, the spatial and temporal adaptive reflectance fusion model (STARFM), to combine 30 m Landsat ETM+ data with daily 500 m MODIS reflectance data. The technique, while providing useful information, requires Landsat scene-dependent tuning parameters and does not explicitly handle the directional dependence of reflectance as a function of the sun-target-sensor geometry, usually described by the Bi-directional Reflectance Distribution Function (BRDF). Temporal plots of MODIS reflectance against time reveal a significant directional reflectance dependence that is well documented (Roy et al., 2002; Schaaf et al., 2002), and for example, remains in MODIS vegetation indices (Gao et al., 2002; Huete et al., 2002). The Landsat sensor, with its comparatively narrow field of view, is not as severely affected by the effects of view angle variations as MODIS, although some impacts have been documented, and even when the Landsat data are atmospherically corrected, seasonal solar zenith variations remain (Danaher et al., 2001; Hansen et al., 2008; Toivonen et al., 2006). Relative and absolute methods to radiometrically normalize Landsat data usually assume implicitly that BRDF variations are negligible or treat them as a source of noise. Normalization methods that correct for these effects have been developed but are not widely used. These include empirical fitting of polynomial functions of reflectance against cross-track pixel location (Hansen et al., 2008), or the inversion of BRDF models and then prediction of reflectance for constant viewing and solar geometry (Danaher et al., 2001). The former requires pseudo-invariant features located across the scene, which may not be available. The latter require several acquisitions needed to reliably characterize the surface BRDF; however, Landsat data are relatively expensive and often unavailable (Ju & Roy, 2008), and increasing the duration between acquisitions to obtain more observations increases the likelihood of violating the inversion assumption that the surface state is static (Gao et al., 2001; Roy et al., 2006).

In this paper a semi-physical fusion approach that uses the MODIS BRDF/Albedo product to describe the surface BRDF modulated by sub-pixel variations at the ETM+ pixel scale is presented. The method is demonstrated for prediction of ETM+ reflectance and may potentially be used for ETM+ cloud and SLC-off gap filling and for the radiometric normalization needed to generate seamless large area mosaic products. Particular advantages of the method are: it does not require any tuning parameters and so may be automated; it is applied on a per-pixel basis and is unaffected by the presence of missing or contaminated neighboring Landsat pixels; and it allows for future improvements through BRDF model refinement and error assessment.

## 2. Method

The MODIS BRDF/Albedo product includes spectral BRDF model parameters that may be used to compute the directional reflectance at any desired view or solar angle (Schaaf et al., 2002). The MODIS BRDF model, Ross-Thick/Li-Sparse-Reciprocal, is a weighted sum of an isotropic parameter and two functions (or kernels) of viewing and illumination geometry and has been shown to be well suited to describing the surface reflectance anisotropy of global land cover types (Lucht et al., 2000; Privette et al., 1997). The kernel weights (spectral BRDF model parameters) are determined as those that best fit all of the cloud-cleared, atmospherically-corrected MODIS reflectances available for each pixel location over a 16-day period (Schaaf et al., 2002). The 16-day period was chosen as an appropriate tradeoff between the availability of sufficient angular samples and the temporal stability of the surface (Gao et al., 2001; Wanner et al., 1997). In the most recent version, Collection 5, the 16-day MODIS BRDF/Albedo product is produced every 8 days with a 500 m pixel dimension from 2000 onwards. Directional observations from MODIS on board both the Terra and Aqua satellites are utilized from mid-2002 onward to increase the probability that sufficient angular samples will be obtained.

The MODIS reflectance  $\hat{r}(\lambda_{\text{MODIS}}, \Omega, \Omega')$  at wavelength  $\lambda_{\text{MODIS}}$  for viewing vector  $\Omega$  and solar illumination vector  $\Omega'$  is modeled as:

$$\hat{r}(\lambda_{\text{MODIS}}, \Omega, \Omega') = f_{\text{iso}}(\lambda_{\text{MODIS}}) + f_{\text{vol}}(\lambda_{\text{MODIS}})K_{\text{vol}}(\Omega, \Omega') + f_{\text{geo}}(\lambda_{\text{MODIS}})K_{\text{geo}}(\Omega, \Omega') \quad (1)$$

where  $K_i(\Omega, \Omega')$  are the BRDF model kernels and  $f_i(\lambda_{\text{MODIS}})$  are the spectral model parameters (Roujean et al., 1992; Schaaf et al., 2002). For locations where the model parameters cannot be confidently retrieved due to poor or insufficient input observations, typically due to persistent cloud obscuration, a backup algorithm is employed (Strugnell & Lucht, 2001; Strugnell et al., 2001). The backup algorithm assumes that the surface directional reflectance can be described by a multiplicative modulation:

$$\hat{r}(\lambda_{\text{MODIS}}, \Omega, \Omega') \approx kA(\lambda_{\text{MODIS}}, \Omega, \Omega') \quad (2)$$

where  $A(\lambda_{\text{MODIS}}, \Omega, \Omega')$  is a modeled reflectance for an archetype temporally constant BRDF 'shape' for a given land cover type (fixed values of the spectral model parameters in Eq. (1)), and  $k$  is a 'scaling' constant that is calculated from three or more MODIS observations. While considered a lower quality result, this MODIS backup algorithm performs well under normal situations (Jin et al., 2003a,b; Salomon et al., 2006).

**Fig. 2.** A 7.5 km × 9 km subset of the Africa scene illustrating a one-way near-infrared (NIR) reflectance prediction. The model predicts November 25th 2001 ETM+ top of atmosphere (TOA) reflectance using observed January 9th 2001 ETM+ TOA reflectance and MODIS surface reflectance modeled for both dates ETM+ geometry (see Eq. (4)).  $a$  is observed January 9th 2001 ETM+ NIR TOA reflectance,  $b$  and  $d$  are modeled January 9th 2001 and November 25th 2001 MODIS NIR surface reflectance at the ETM+ geometries of the two dates respectively,  $c$  is observed November 25th 2001 ETM+ NIR TOA reflectance,  $e$  is predicted November 25th 2001 ETM+ NIR TOA reflectance ( $e=a \cdot (d/b)$ ),  $f$  is the temporal residual (absolute value of  $a - c$ ), and  $g$  is prediction residual (absolute value of  $e - c$ ), and  $h$  is where the prediction residual is greater than temporal residual (in black). Figures  $a$ ,  $b$ ,  $c$ ,  $d$ , and  $e$  are shown with the same contrast stretch. Residual values in  $f$  and  $g$  are colored as:  $0 \leq \text{purple} < 0.015$ ,  $0.015 \leq \text{blue} < 0.03$ ,  $0.03 \leq \text{green} < 0.045$ ,  $0.045 \leq \text{yellow} < 0.06$ ,  $0.06 \leq \text{orange} < 0.09$ ,  $\text{red} \geq 0.09$ .

**Table 4**

African study site summary statistics: predicting November 25th 2001 ETM+ top of atmosphere (TOA) reflectance using January 9th 2001 ETM+ TOA reflectance data and contemporaneous MODIS products (Tables 2 and 3)

	Band 1	Band 2	Band 3	Band 4	Band 5	Band 7
$\bar{\Delta}_{\text{temporal}}$	0.024	0.017	0.024	0.063	0.019	0.022
$\Delta_{\text{temporal}}$	0.293	0.243	0.462	0.245	0.121	0.324
$\bar{\Delta}_{\text{prediction}}$	0.014	0.016	0.009	0.024	0.015	0.010
$\Delta_{\text{prediction}}^*$	0.171	0.229	0.173	0.093	0.096	0.147
$\bar{\Delta}_{\text{prediction}}/\bar{\Delta}_{\text{temporal}} = \Delta_{\text{prediction}}^*/\Delta_{\text{temporal}}^*$	0.58	0.94	0.38	0.38	0.79	0.45
2001/11/25 mean TOA reflectance	0.082	0.070	0.052	0.257	0.158	0.068

$\bar{\Delta}_{\text{temporal}}$  is the mean temporal residual,  $\Delta_{\text{temporal}}^*$  is mean reflectance normalized temporal residual,  $\bar{\Delta}_{\text{prediction}}$  is the mean prediction residual,  $\Delta_{\text{prediction}}^*$  is mean reflectance normalized prediction residual (see text for details).

The formulation (2) implies that:

$$\frac{\hat{\rho}_{t2}(\lambda_{\text{MODIS}}, \Omega_2, \Omega'_2)}{\hat{\rho}_{t1}(\lambda_{\text{MODIS}}, \Omega_1, \Omega'_1)} \approx \frac{k_{t2} A(\lambda_{\text{MODIS}}, \Omega_2, \Omega'_2)}{k_{t1} A(\lambda_{\text{MODIS}}, \Omega_1, \Omega'_1)} = c \quad (3)$$

where  $\hat{\rho}_{ti}(\lambda_{\text{MODIS}}, \Omega_i, \Omega'_i)$  is the MODIS reflectance at time  $t_i$  for angles  $\Omega_i, \Omega'_i$ ; that is MODIS reflectance temporal dynamics can be approximated by the multiplicative modulation term  $c$ .

We assume that the MODIS modulation term  $c$  for  $\lambda_{\text{MODIS}}$  is representative of the reflectance variation at Landsat ETM+ scale for a spectrally similar Landsat ETM+ wavelength  $\lambda_{\text{ETM+}}$ . Thus, prediction of Landsat reflectance at time  $t_2$  from a Landsat observation at time  $t_1$  is defined:

$$\rho_{\text{ETM+}, t2}(\lambda_{\text{ETM+}}, \Omega_{\text{new}}, \Omega'_{\text{new}}) = c \times \rho_{\text{ETM+}, t1}(\lambda_{\text{ETM+}}, \Omega_{\text{observed}}, \Omega'_{\text{observed}}) \quad (4)$$

$$c = \frac{\hat{\rho}_{\text{MODIS}, t2}(\lambda_{\text{MODIS}}, \Omega_{\text{new}}, \Omega'_{\text{new}})}{\hat{\rho}_{\text{MODIS}, t1}(\lambda_{\text{MODIS}}, \Omega_{\text{observed}}, \Omega'_{\text{observed}})}$$

where  $\hat{\rho}_{\text{ETM+}, t2}(\lambda_{\text{ETM+}}, \Omega_{\text{new}}, \Omega'_{\text{new}})$  is the modeled Landsat reflectance for ETM+ wavelength  $\lambda_{\text{ETM+}}$  for any desired viewing and solar illumination vectors  $\Omega_{\text{new}}, \Omega'_{\text{new}}$  at time  $t_2$ ,  $\rho_{\text{ETM+}, t1}(\lambda_{\text{ETM+}}, \Omega_{\text{observed}}, \Omega'_{\text{observed}})$  is the reflectance of a Landsat observation of the pixel sensed at time  $t_1$  with viewing and solar illumination vectors  $\Omega_{\text{observed}}, \Omega'_{\text{observed}}$ , and  $\hat{\rho}_{\text{MODIS}}$  is the modeled reflectance for these angles computed at coarser spatial resolution using the MODIS BRDF/Albedo product.

If the assumption that the MODIS modulation term  $c$  is representative of the reflectance variation at Landsat ETM+ scale holds, then the method should accommodate temporal variations due to surface changes (e.g., phenological, land cover/land use variations) that are observable at the MODIS BRDF/Albedo product resolution. This assumption implies that over a MODIS pixel dimension the standard deviation and mean Landsat reflectance at time  $t_2$  are a factor of  $c$  times those at  $t_1$ . A feature arising from this assumption is that the ratio of the Landsat reflectance standard deviation and mean, i.e. the coefficient of variation, is constant between the two times. This may not occur when there are processes acting to change reflectance in a spatially heterogeneous manner at scales larger than the 30 m Landsat pixels and smaller than the 500 m MODIS pixels, for example due to natural or human processes (Lambin, 1999) and/or due to image misregistration and resampling artifacts (Roy & Dikshit, 1994).

Since the MODIS BRDF/Albedo product provides near-spatially and near-temporally complete global coverage, Landsat reflectance can be predicted at any date after the first MODIS product availability in February 2000 (Justice et al., 2002; Schaaf et al., 2002). In this way, Landsat ETM+ reflectance can be predicted when an ETM+ pixel is cloud obscured or missing due to the ETM+ scan line corrector problem. The method may also be used for relative radiometric normalization. The only requirements to compute Eq. (4) for an uncontaminated ETM+ pixel, are the solar and viewing geometry for the pixel on the uncontaminated and predicted dates, and representative MODIS BRDF spectral model parameters for the two dates. What constitutes “representative” is an open research question, but certainly the optimal solution would be to

use the highest spatial resolution MODIS BRDF model parameters that are temporally and spatially coincident with the Landsat acquisition dates and locations respectively. In this way the MODIS modeled reflectance is predicted at similar viewing and illumination angles and under similar atmospheric and surface conditions as the Landsat data for the two dates. If multiple Landsat acquisitions are available, a temporal weighting of Eq. (4) may be used to interpolate Landsat reflectance between dates. A simple linear temporal weighting scheme could be applied, or more sophisticated methods developed, e.g., based on observed MODIS reflectance temporal dynamics.

This approach is computationally efficient to implement as the BRDF spectral model parameters are provided by the MODIS BRDF/Albedo product suite. It is applied independently on a Landsat per-pixel basis, is unaffected by the presence of missing or contaminated neighboring Landsat pixels, and may be automated without the requirement for any tuning parameters.

### 3. Data

#### 3.1. Landsat data

Landsat ETM+ L1G data processed by the Level 1 Product Generation System at the United States Geological Survey (USGS) Center for Earth Resources Observation and Science (EROS) are used. The L1G data are not atmospherically corrected and are geometrically corrected only to remove systematic geometric errors related to the sensor, satellite and Earth (WWW1). Each Landsat scene covers an area of approximately 183 km × 170 km defined in the UTM coordinate system and referenced by a unique Landsat Worldwide Reference System (WRS-2) path and row coordinate (Arvidson et al., 2001). In this study the 30 m blue (0.45–0.52 μm), green (0.53–0.61 μm), red (0.63–0.69 μm), near-infrared (0.78–0.90 μm), and the two mid-infrared (1.55–1.75 μm and 2.09–2.35 μm) bands are used; the thermal infrared and panchromatic bands are not used (Table 1).

#### 3.2. MODIS data

The 16-day MODIS BRDF/Albedo model parameter product (MCD43A1) is used to compute the directional reflectance at any desired viewing and solar geometry for six of the seven MODIS 500 m land surface reflectance bands: blue (0.459–0.479 μm), green (0.545–0.565 μm), red (0.620–0.670 μm), near-infrared (0.841–0.876 μm) and middle-infrared (1.628–1.654 μm and 2.105–2.155 μm); the MODIS 1.230–1.250 μm middle-infrared band is not used since it has no corresponding ETM+ band. The MODIS BRDF/Albedo quality product (MCD43A2) describes the per-pixel band-specific BRDF model inversion quality quantized into 5 values coded 0–4 indicating decreasing inversion quality. Full inversions (number of valid observations >=7) are coded as 0 and 1 indicating the “best” (uncertainty in modeled reflectance small for most of the observations) and “good” quality inversions respectively. Less reliable magnitude inversions computed using the backup algorithm are coded as 2 (number of valid observations >=7 but full inversion quality only moderate) or 3

**Table 5**

African study site summary statistics: predicting January 9th 2001 ETM+ top of atmosphere (TOA) reflectance using November 25th 2001 TOA reflectance ETM+ data and contemporaneous MODIS products (Tables 2 and 3)

	Band 1	Band 2	Band 3	Band 4	Band 5	Band 7
$\bar{\Delta}_{\text{temporal}}$	0.024	0.017	0.024	0.063	0.019	0.022
$\Delta_{\text{temporal}}$	0.226	0.195	0.316	0.325	0.115	0.250
$\bar{\Delta}_{\text{prediction}}$	0.022	0.016	0.011	0.018	0.015	0.012
$\Delta_{\text{prediction}}^*$	0.208	0.184	0.145	0.093	0.091	0.136
$\bar{\Delta}_{\text{prediction}}/\bar{\Delta}_{\text{temporal}} = \Delta_{\text{prediction}}^*/\Delta_{\text{temporal}}^*$	0.92	0.94	0.46	0.29	0.79	0.55
2001/01/09 mean TOA reflectance	0.106	0.087	0.076	0.194	0.165	0.088

(number of valid observations  $>=3$  and  $<7$ ), and pixels where there were insufficient observations for BRDF inversion are coded as 4. The MODIS BRDF/Albedo products are defined in  $10^\circ \times 10^\circ$  tiles in the equal area sinusoidal projection (Wolfe et al., 1998).

Only the most recently processed Collection 5 MODIS BRDF/Albedo products are used as these reflect the latest improvements to the MODIS science algorithms, calibration, geolocation and production code, and are defined at 500 m rather than at 1 km as in previous collections. In addition, for Collection 5, a quasi-rolling production strategy, where the 16-day product is produced every 8 days on an 8-day overlapping basis was adopted to maximize cloud-free retrievals while minimizing global data processing constraints (Roy et al., 2006) enabling more precise temporal correspondence between the MODIS BRDF/Albedo and the Landsat data used in this study.

### 3.3. Study sites and satellite data

Three study sites, one in Africa and two in the U.S., were selected, each defined by the extent of a Landsat 183 km  $\times$  170 km scene (Tables 2

and 3). Two Landsat acquisitions and the spatially and temporally coincident 16-day MCD43A1/2 product instances were selected for each site. Only Landsat acquisitions with low cloud cover were selected in order to maximize the number of cloud-free pixels, and to reduce the number of low quality MODIS BRDF/Albedo product values. The data were selected from 2000 and 2001 in order to utilize the most recently processed (at the time of writing) Collection 5 MODIS BRDF/Albedo data

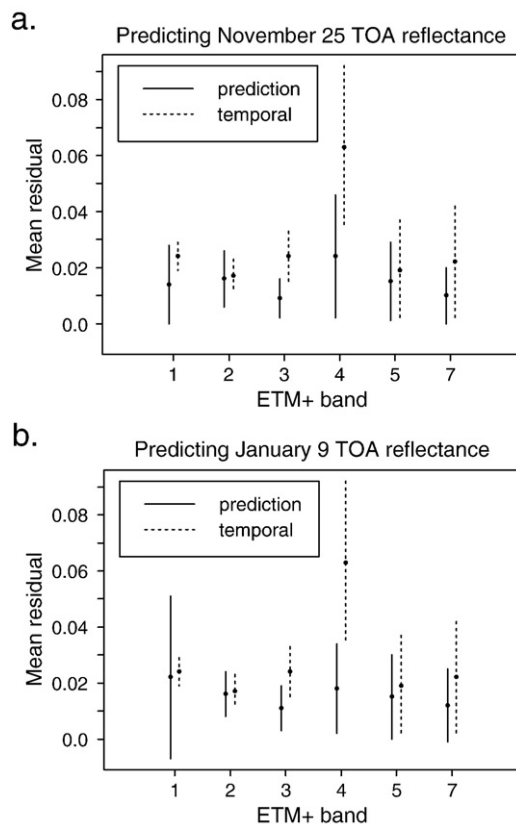


**Fig. 3.** Mean and plus/minus one standard deviation of the prediction residuals (solid lines) and temporal residuals (dotted lines) in predicting (a) November 25th 2001 and (b) January 9th 2001 reflectance, for the six top of atmosphere reflective bands of the African Landsat data. The temporal residuals for each band are the same for the two prediction directions in (a) and (b) by definition.

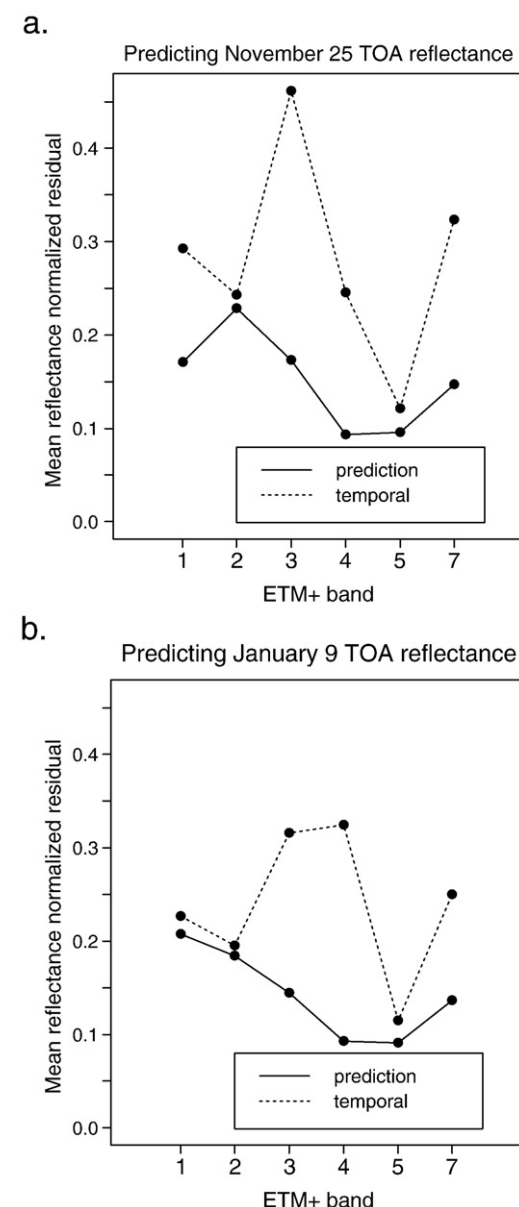


**Fig. 4.** Mean reflectance normalized prediction residuals (solid lines) and temporal residuals (dotted lines) in predicting (a) November 25th 2001 and (b) January 9th 2001 reflectance, for the six top of atmosphere reflective bands of the African Landsat data.

products. Consequently, as Aqua was not yet launched, only Terra observations were used by the MODIS BRDF/Albedo product. Spatially, the sites encompass a range of land cover/land use types and relief variations; temporally, the selected dates capture temporal variations in the solar illumination, phenology and land use/land cover.

The Africa site is located near the Equator with the majority of the scene falling in the Democratic Republic of the Congo and small portions in southern Sudan and northwestern Uganda. Fig. 1a illustrates the site showing land cover classes defined by the MODIS land cover product (Friedl et al., 2002) with predominantly woody savanna across much of the scene, tropical evergreen broadleaf forests in the Southwest, and fragmented open shrublands and croplands in the Northeast. Two Landsat acquisitions and the contemporaneous MODIS BRDF/Albedo products were selected from around the end of the dry season (January 9th ETM+ acquisition) and the beginning of the following wet season (November 25th ETM+ acquisition) with mean NDVI of 0.59 and 0.75 respectively; where the NDVI was derived from MODIS nadir BRDF-adjusted reflectance (NBAR) red and near-infrared reflectance computed as Eq. (1) for a nadir view and for the solar zenith angle at the centre of the Landsat scene.

The two U.S. sites touch in one corner and are located primarily in Oregon and Idaho respectively. Both sites are characterized by substantial proportions of mountainous terrain covered by evergreen needle-leaf forest, grasslands and shrublands (Fig. 1b and c). The Oregon Landsat data were acquired June 16 and October 6 2000, with MODIS nadir BRDF-adjusted reflectance (NBAR) derived mean NDVI of 0.50 and 0.41 respectively. The Idaho acquisitions were acquired July 11 and September 13 2000, with mean NBAR NDVI of 0.66 and 0.55 respectively.

The Idaho site has a greater proportion of croplands (~15%) than the Oregon site (~3%) and the majority of agricultural harvesting occurred in both sites by the time of the second Landsat acquisition.

#### 4. Data pre-processing

##### 4.1. Landsat angular geometry computation

To implement the method developed above, the Landsat viewing vector ( $\Omega$  = view zenith angle, view azimuth angle) and the solar illumination vector ( $\Omega'$  = solar zenith angle, solar azimuth angle) must be defined for each Landsat pixel. The solar illumination vector was computed using an astronomical model parameterized for geodetic latitude and longitude and time following the approach developed for MODIS geolocation (Standish et al., 1992; Wolfe et al., 2002; WWW2). The viewing vector was derived using the Image Assessment System (IAS) geometric libraries developed to monitor, characterize, and calibrate sensor and platform specific aspects of the Landsat 7 satellite and ETM+ sensor (Lee et al., 2004). The IAS provides the capability to create Level 1, or systematic products from Level 0R, or geometrically raw data, using payload correction, mirror scan, and calibration parameter data. Optional IAS post-processing of satellite ephemeris was also used as this is more accurate than the ephemeris information downlinked directly with the Landsat 7 telemetry (WWW1). Geometric errors due to terrain relief displacement were not accounted for. The viewing vector was computed for each output pixel in the Level 1G product by first computing a vector normal to the surface of the WGS84 Earth model for the geodetic pixel coordinate, then the unit vector from

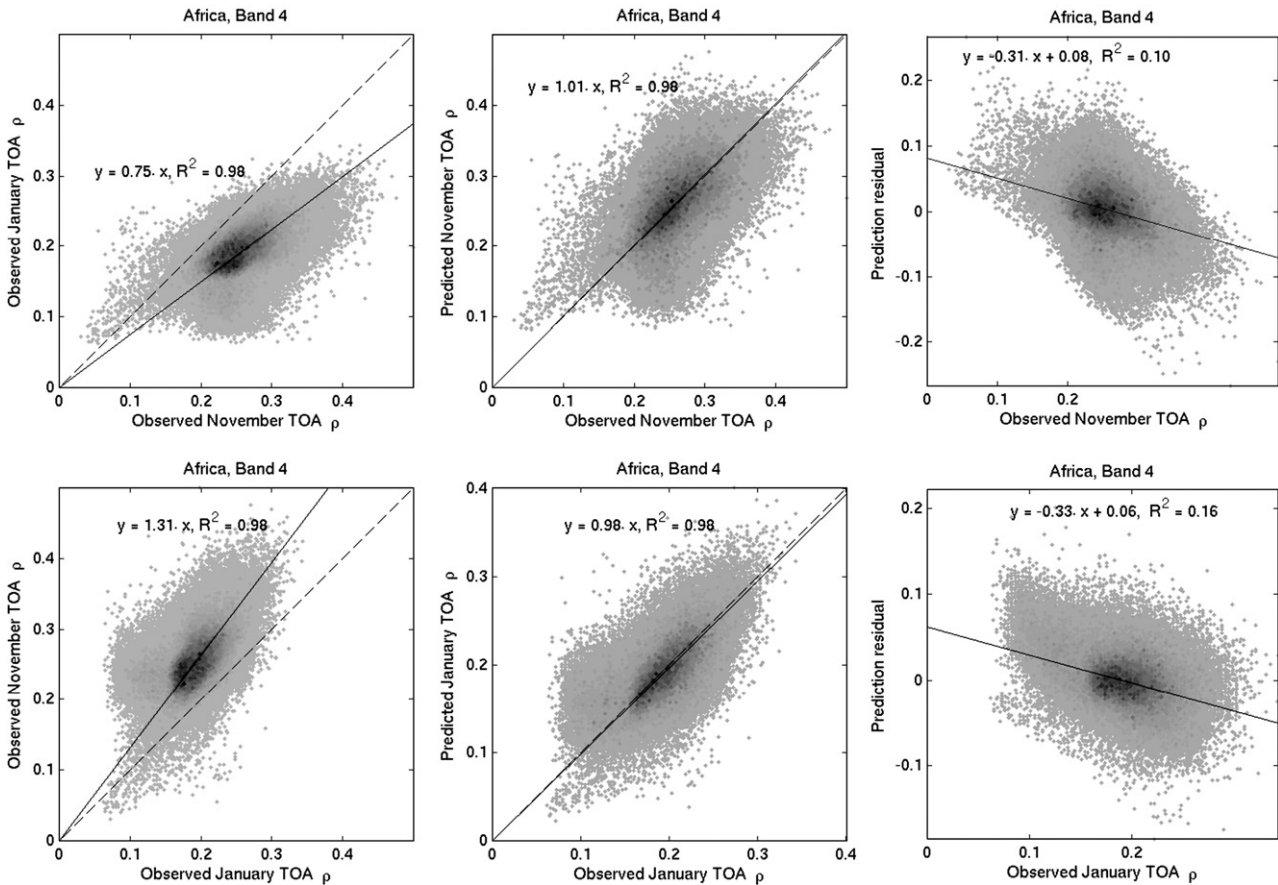


**Fig. 5.** Scatterplots of the African scene top of atmosphere (TOA) near-infrared (band 4) reflectance, showing observed versus predicted reflectance, and prediction residuals versus observed reflectance, for the two acquisition dates November 25th 2001 and January 9th 2001. The top row illustrates prediction of November 25th reflectance, and the bottom row illustrates prediction of January 9th reflectance. A simple regression line through the origin of these data is shown superimposed (solid line). Because of the large number of 30 m pixels, these data are shown for 30 m pixels sampled regularly every 10 rows and 10 columns from across the image; 289,210 pixels are illustrated. The frequency of occurrence of pixels with the same reflectance is illustrated by density shading with darker tones illustrating higher frequency of occurrence.

the geodetic coordinate to the modeled satellite position, adjusting for the sensor-satellite attitude, and then the viewing vector zenith and azimuth components derived using standard trigonometric formulae.

The required accuracy for the Landsat viewing and solar illumination vector is an open research question as the impact of angular errors is a function of the surface anisotropy as well as the angles and their uncertainties (Roy & Singh, 1994). Uncertainties in the Landsat viewing and solar illumination vector will be greatest in non-flat regions as no terrain correction was undertaken. In general however, we expect achievable angular errors less than a degree will in most cases be acceptable, as only when data are sensed near the BRDF hot-spot will angular errors of this magnitude result in significant reflectance changes (Lacaze & Roujean, 2001; Vermote & Roy, 2002).

#### 4.2. Reflectance computation

The impact of the atmosphere on satellite observations is variable in space and time and is usually considered as requiring correction for quantitative remote sensing applications (Liang et al., 2002; Ouaidrari & Vermote, 1999; Vermote et al., 2002). The Landsat reflective band data (Table 1) were converted from digital numbers to top of atmosphere (TOA) reflectance using the best available ETM+ calibration coefficients and standard correction formulae taking into account the Sun-Earth distance and using the per-pixel solar zenith angle data. The solar zenith angle (Section 4.1) is taken here as being relative to a level surface, and so may be biased over mountainous terrain.

Several Landsat atmospheric correction methods have been proposed, with the Dense Dark Vegetation (DDV) approach (Kaufman et al., 1997) used because it enables correction for aerosol effects that are

highly variable and not well characterized by atmospheric climatological data (Ouaidrari & Vermote, 1999). The DDV approach is based on empirical relationships between the visible and mid-infrared bands for dense dark vegetation to estimate aerosol optical depth (AOD). In this study we use the relationship  $\rho_1 = 0.33\rho_7$ , where  $\rho_1$  and  $\rho_7$  are Landsat band 1 and 7 surface reflectance (Masek et al., 2006). Standard, mid-latitude summer climatologies for water vapor and ozone concentration, and air pressure parameterized from the mean surface elevation, were used to correct the band 7 TOA reflectance using the 6S vectorized radiative transfer code (Kotchenova et al., 2006). DDV pixels were defined as those pixels not labeled as cloud or shadow (Section 4.3), and with  $0.02 \leq \rho_7 \leq 0.05$ ; these specific thresholds were determined by visual inspection to select only dense forest candidates. The mean band 1 TOA reflectance,  $\bar{\rho}_1^*$ , and the mean band 7 surface reflectance,  $\bar{\rho}_7$ , for DDV pixels falling within 1 km grids were computed (Masek et al. 2006) and used to invert for AOD using 6S, iteratively varying AOD with a 0.01 step and atmospherically correcting  $\bar{\rho}_1^*$  until  $\bar{\rho}_1 \approx 0.33\bar{\rho}_7$ . The median of the AODs estimated within the Landsat scene was then used, with a continental aerosol model, and the standard, mid-latitude summer climatology data, to atmospherically correct the Landsat TOA reflectance data using 6S. Use of a median AOD value, rather than spatially interpolating the AOD across the scene, will introduce some error, but is likely to provide a more reliable atmospheric correction than more simple dark object subtraction techniques (Chavez, 1996).

Surface reflectances were computed in this way for the two U.S. scenes. Atmospheric correction was not undertaken for the Africa Landsat acquisitions because of difficulties in reliably identifying DDVs; only a small proportion of the scene was composed of dense forest (Fig. 1a) and many of the forest pixels were cloud contaminated. Results

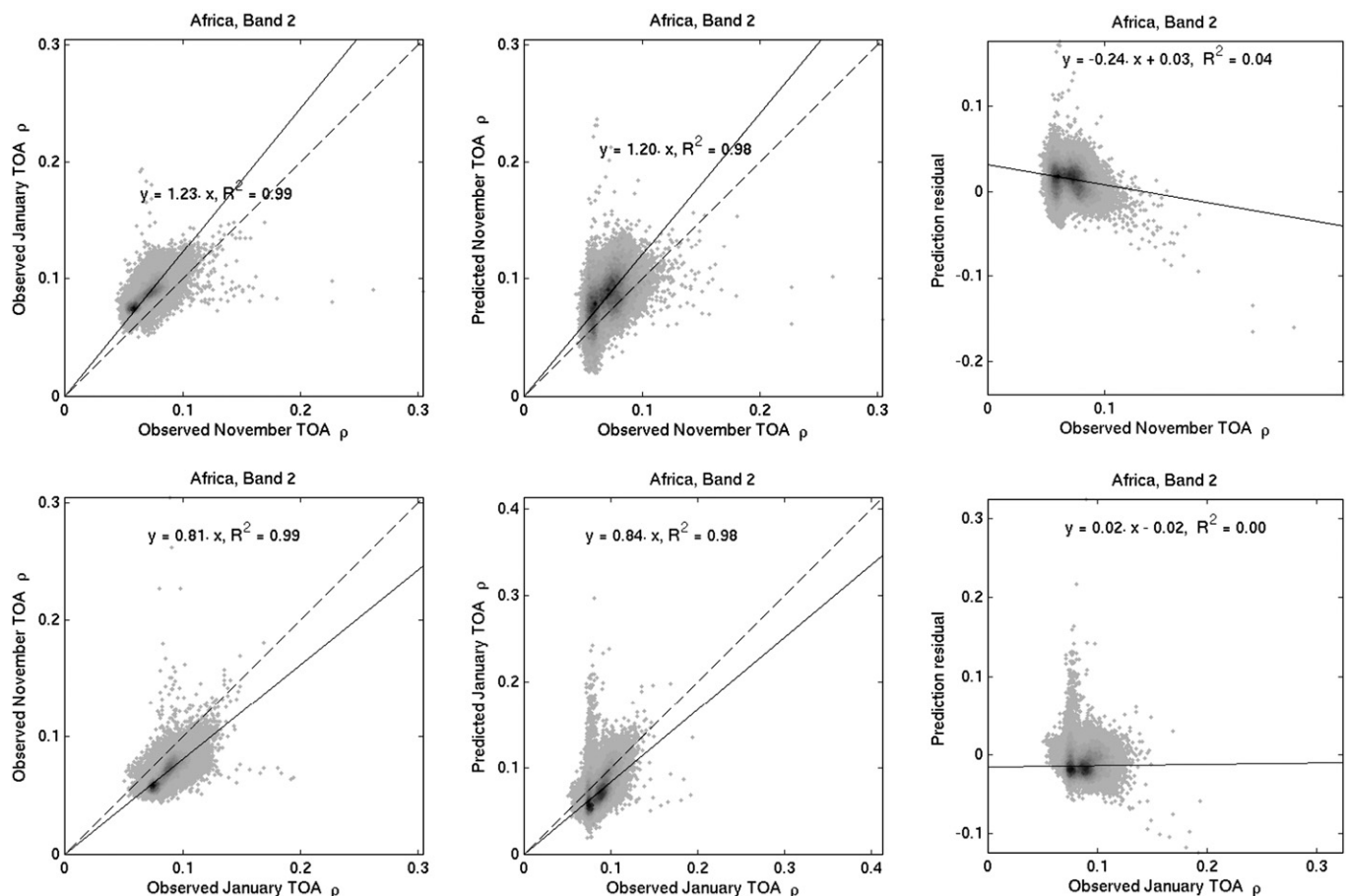


**Fig. 6.** Scatterplots of the African scene TOA green (band 2) reflectance, showing observed versus predicted reflectance, and prediction residuals versus observed reflectance, for the two acquisition dates November 25th 2001 and January 9th 2001. See Fig. 5 caption for further details.

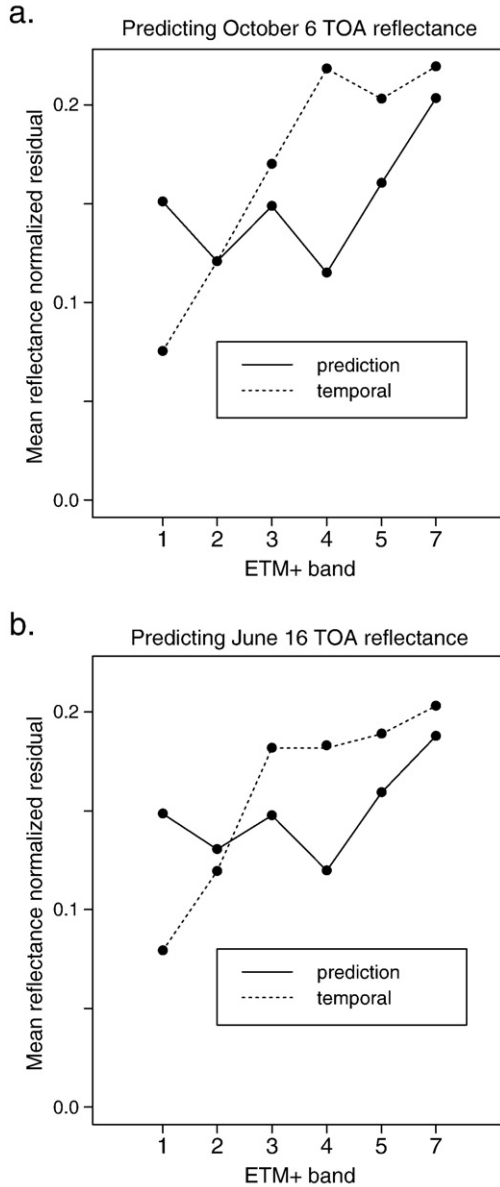


**Fig. 7.** Mean reflectance normalized prediction residuals (solid lines) and temporal residuals (dotted lines) in predicting (a) October 6th 2000 and (b) June 16th 2000 reflectance, for the 6 reflective bands of the Oregon Landsat data without 6S correction, i.e., TOA reflectance.

for the U.S. sites, with and without the 6S correction, are shown to investigate the sensitivity of the approach to atmospheric contamination.

The MODIS BRDF/Albedo products are generated from atmospherically-corrected MODIS reflectance (Vermote et al., 2002) and so do not need correction for atmospheric effects. MODIS surface reflectance was computed from Eq. (1) for the six MODIS bands used in this study (Table 1).

#### 4.3. Cloud and cloud shadow masking

It is well established that optically thick clouds preclude optical wavelength remote sensing of the land surface (Kaufman, 1987) and that cloud shadows deleteriously contaminate surface reflectance (Asner & Warner, 2003). Automated methods for flagging clouds and cloud shadows are a requirement for large-volume processing of MODIS (Ackerman et al., 1998; Platnick et al., 2003) and Landsat data (Helmer & Ruefenacht, 2005; Irish et al., 2006).

In this study, the U.S. Landsat acquisitions have minimal cloud content (Table 2) and so residual clouds and cloud shadows were identified by visual inspection and masked off manually. Clouds and cloud shadows were identified in the African Landsat acquisitions using a supervised classification tree approach prototyped for Landsat mapping of the Congo River basin (Hansen et al., 2008). Photo-interpreted training sets were extracted manually from the Landsat data. The Landsat near-infrared (0.78–0.90 μm), mid-infrared (1.55–1.75 μm and 2.09–2.35 μm) and thermal (10.4–12.5 μm) bands, and all combinations of possible 2 band simple ratios, were used as inputs to separate cloud and cloud shadow classification trees. Class membership likelihood values from a classification tree bagging procedure (Breiman, 1996) were used to define for each pixel the cloud and shadow likelihood and then thresholded conservatively to produce spatially explicit cloud and shadow binary masks.

The MODIS BRDF/Albedo product is sensitive to cloud contamination, and in regions of persistent cloud there may be insufficient

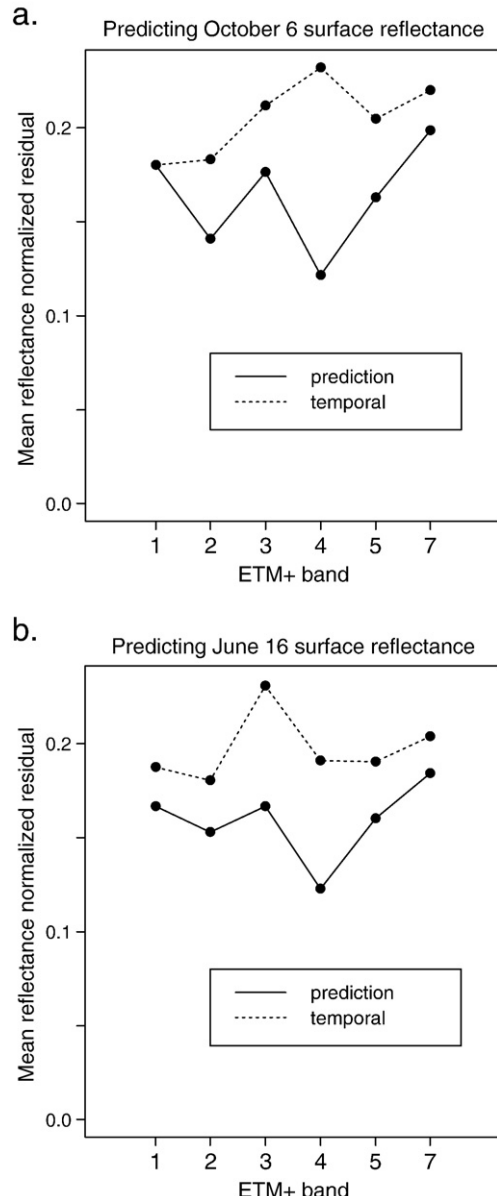


**Fig. 8.** Mean reflectance normalized prediction residuals (solid lines) and temporal residuals (dotted lines) in predicting (a) October 6th 2000 and (b) June 16th 2000 reflectance, for the 6 reflective bands of the Oregon Landsat data with 6S correction, i.e. surface reflectance.

**Table 6**

Oregon study site summary statistics: predicting October 6th 2000 ETM+ 6S corrected surface reflectance using June 16th 2000 ETM+ 6S corrected surface reflectance data and contemporaneous MODIS products (Tables 2 and 3)

	Band 1	Band 2	Band 3	Band 4	Band 5	Band 7
$\bar{\Delta}_{\text{temporal}}$	0.009	0.013	0.018	0.042	0.044	0.031
$\Delta_{\text{temporal}}^*$	0.180	0.183	0.212	0.232	0.205	0.220
$\bar{\Delta}_{\text{prediction}}$	0.009	0.010	0.015	0.022	0.035	0.028
$\Delta_{\text{prediction}}^*$	0.180	0.141	0.176	0.122	0.163	0.199
$\bar{\Delta}_{\text{prediction}}/\bar{\Delta}_{\text{temporal}} = \Delta_{\text{prediction}}^*/\Delta_{\text{temporal}}^*$	1.00	0.77	0.83	0.52	0.80	0.90
2000/10/06 mean surface reflectance	0.050	0.071	0.085	0.181	0.215	0.141

observations to undertake BRDF model inversion (Moody et al., 2005; Schaaf et al., 2002). Although the MODIS BRDF/Albedo processing software rejects MODIS observations labeled as cloudy and a reiterative retrieval approach is implemented to remove obvious outliers, residual cloud, and cloud shadow contamination may remain in the backup retrievals. Cloud and cloud shadow contaminated data reduce the reliability of the BRDF model inversion and their presence is reflected indirectly in the per-pixel inversion quality assessment data.

#### 4.4. Landsat and MODIS geometric registration

The MODIS geolocation error is approximately 50 m ( $1\sigma$ ) at nadir (Wolfe et al., 2002) and the Landsat L1G geolocation error is less than 250 m ( $1\sigma$ ) and comparable to the MODIS error in areas of flat relief when post-processing of satellite ephemeris is used (Lee et al., 2004). Considerable effort was taken to ensure that these data were precisely co-registered, and reprojected in a way that preserved the integrity of the Landsat solar and viewing geometry and the MODIS BRDF/Albedo model parameter and quality assessment values.

The two Landsat ETM+ acquisitions were first compared visually at each site to ensure that they were co-registered correctly in the UTM coordinate system. The African acquisitions were misregistered by about one 30 m pixel in both the X and Y axes and so one acquisition was translated by this amount. In this way, the Landsat acquisitions at each study site were judged visually to be co-registered to within one 30 m ETM+ pixel.

Next, the 500 m MODIS BRDF/Albedo products (MCD43A1 and MCD43A2) were reprojected from the MODIS sinusoidal projection into registration with the Landsat UTM projection. The MODIS data were reprojected using the MODIS Reprojection Tool (WWW3) with nearest-neighbor resampling to maintain the MODIS pixel values and 30 m output pixel dimensions to reduce nearest-neighbor resampling pixel shifts (i.e., position errors) (Roy & Dikshit, 1994). The African and U.S. Idaho Landsat scenes encompass two MODIS tiles and so both MODIS tiles were reprojected (Table 3). Finally the contemporaneous MODIS and Landsat data, both defined with 30 m pixels in the UTM coordinate system, were visually compared to check that they were co-registered correctly. The comparison was of the spectrally similar near-infrared MODIS and Landsat bands, focusing on regions containing distinct features. Subsequently, the U.S. MODIS 30 m data were translated by between 9 and 17 30 m pixels in each axes to provide the best Landsat-MODIS co-registration. No adjustment was performed for the Africa data as none was deemed necessary.

#### 5. Accuracy analysis

To demonstrate the method, the reflectance in both temporal directions is predicted as Eq. (4) at each study site; that is, the ETM+ reflectance for the viewing and solar illumination geometry at date  $a$  is predicted using date  $b$  ETM+ data, and conversely, the reflectance for the viewing and solar illumination geometry at date  $b$  is predicted using date  $a$  ETM+ data (dates are defined in Tables 2 and 3). Predictions are undertaken for Landsat bands 1, 2, 3, 4, 5, 7 using the spectrally nearest MODIS band (Table 1).

The residual difference between the predicted and observed reflectance at an ETM+ pixel is computed for each ETM+ spectral band as:

$$\Delta_{\text{prediction},\lambda}(\lambda_{\text{ETM+}}, i, j) = |\hat{\rho}_{\text{date } a}(\lambda_{\text{ETM+}}, i, j) - \rho_{\text{date } a}(\lambda_{\text{ETM+}}, i, j)| \quad (5)$$

where  $\Delta_{\text{prediction}}$  is termed the prediction residual, i.e., the absolute value of the difference between the predicted reflectance  $\hat{\rho}_{\text{date } a}(\lambda_{\text{ETM+}}, i, j)$  (Eq. (4)) and the observed reflectance  $\rho_{\text{date } a}(\lambda_{\text{ETM+}}, i, j)$  at pixel location  $(i, j)$  for date  $a$  (or date  $b$  when the prediction is in the other temporal direction). The residual is defined in unitless reflectance (scaled 0–1).

The residual difference between the reflectance observed on the two dates is also computed for each ETM+ spectral band as:

$$\Delta_{\text{temporal},\lambda}(\lambda_{\text{ETM+}}, i, j) = |\rho_{\text{date } a}(\lambda_{\text{ETM+}}, i, j) - \rho_{\text{date } b}(\lambda_{\text{ETM+}}, i, j)| \quad (6)$$

where  $\Delta_{\text{temporal}}$  is termed the temporal residual, i.e., the absolute value of the difference between the observed reflectance at pixel location  $(i, j)$  for date  $a$  and date  $b$ . The value of  $\Delta_{\text{temporal}}$  will be zero if there are no temporal variations due to surface changes (e.g., phenological, land cover/land use variations) or due to variations imposed by the remote sensing process (e.g., differences in illumination and observation angles, atmospheric contamination, sensor calibration/degradation changes, sensor noise).

To enable the residuals computed in either temporal direction to be compared meaningfully, only pixels where predictions can be computed in both directions are considered. That is, only 30 m pixel locations with valid Landsat data (i.e. not cloud or cloud shadow) and valid 30 m resampled MODIS MCD43 data (i.e. non fill values) on both dates are considered. On average about 30, 36 and 37 million 30 m pixels for the Africa, Oregon and Idaho study sites are considered respectively.

**Table 7**

Oregon study site summary statistics: predicting June 16th 2000 ETM+ 6S corrected surface reflectance using October 6th 2000 ETM+ 6S corrected surface reflectance data and contemporaneous MODIS products (Tables 2 and 3)

	Band 1	Band 2	Band 3	Band 4	Band 5	Band 7
$\bar{\Delta}_{\text{temporal}}$	0.009	0.013	0.018	0.042	0.044	0.031
$\Delta_{\text{temporal}}^*$	0.188	0.181	0.231	0.191	0.190	0.204
$\bar{\Delta}_{\text{prediction}}$	0.008	0.011	0.013	0.027	0.037	0.028
$\Delta_{\text{prediction}}^*$	0.167	0.153	0.167	0.123	0.160	0.184
$\bar{\Delta}_{\text{prediction}}/\bar{\Delta}_{\text{temporal}} = \Delta_{\text{prediction}}^*/\Delta_{\text{temporal}}^*$	0.89	0.85	0.72	0.64	0.84	0.90
2000/06/16 mean surface reflectance	0.048	0.072	0.078	0.220	0.231	0.152

Summary statistics (mean and standard deviation) of  $\Delta_{\text{prediction}}$  and  $\Delta_{\text{temporal}}$  are derived over each study area. In order to be able to inter-compare the mean residuals between spectral bands, mean reflectance normalized residuals are derived as:

$$\begin{aligned}\Delta_{\text{prediction},\lambda}^* &= \frac{\bar{\Delta}_{\text{prediction},\lambda}}{\bar{\rho}_\lambda} \\ \Delta_{\text{temporal},\lambda}^* &= \frac{\bar{\Delta}_{\text{temporal},\lambda}}{\bar{\rho}_\lambda}\end{aligned}\quad (7)$$

where  $\bar{\Delta}_{\text{prediction}}$  and  $\bar{\Delta}_{\text{temporal}}$  are the means of the residual values, Eqs. (5) and (6), and  $\bar{\rho}_\lambda$  is the mean observed reflectance on the predicted date. If the method developed is reliable, then the prediction residuals should be smaller than the temporal residuals, even when observed reflectance changes due to surface variations are significant compared to changes imposed by the remote sensing process.

## 6. Results

Results are first presented for each study site, comparing the prediction and temporal residuals, followed by a detailed illustration of how the methodology handles significant temporal change. An assessment of the prediction residuals with respect to the MODIS BRDF model parameter quality is then described.

### 6.1. African study site results

Fig. 2 illustrates for a 7.5 km × 9 km spatial subset how the method works for a one-way prediction; specifically how November 25th ETM+

TOA reflectance is predicted (Eq. (4)) from the observed January 9th TOA reflectance using the modeled MODIS surface reflectance derived (Eq. (1)) for the ETM+ viewing and solar geometry on these two dates. The results are for the near-infrared (NIR) reflectance bands (Table 1). The ETM+ and MODIS reflectances are illustrated using the same contrast stretch. The subset is of a predominantly woody savanna region, with areas of thick forest (higher reflectance) interspersed within woody grasslands (lower reflectance); a small proportion (~1%) of the woody grasslands burned (lowest reflectance) by January 9th (top row). The observed ETM+ and the modeled MODIS NIR reflectance are darker on January 9th 2001 (top row) than November 25th 2001 (middle row) reflecting phenological differences. The different spatial resolutions of the 30 m ETM+ and the 500 m MODIS data are clearly apparent, for example, the river observed in the North of the ETM+ data is barely discernable in the corresponding MODIS 500 m data.

The observed (Fig. 2c) and predicted (Fig. 2e) November 25th ETM+ reflectances are highly similar in both magnitude and spatial structure. The use of the 500 m resolution MODIS data in the prediction is evident however; the predicted 30 m reflectance appears blocky in certain places corresponding to the pixel boundaries of the (nearest-neighbor resampled) 500 m MODIS modeled reflectance (Fig. 2b and d). The temporal residuals (Eq. (6)) and the prediction residuals (Eq. (5)) are shown on the bottom row of Fig. 2 and are displayed using the same color map. In general, the prediction residuals (Fig. 2g) are considerably lower than the temporal residuals (Fig. 2f) with mean residuals of 0.024 and 0.070 respectively that correspond to 9% and 26% of the mean observed NIR November 25th reflectance (0.271). Fig. 2h shows where the prediction residuals are greater than the

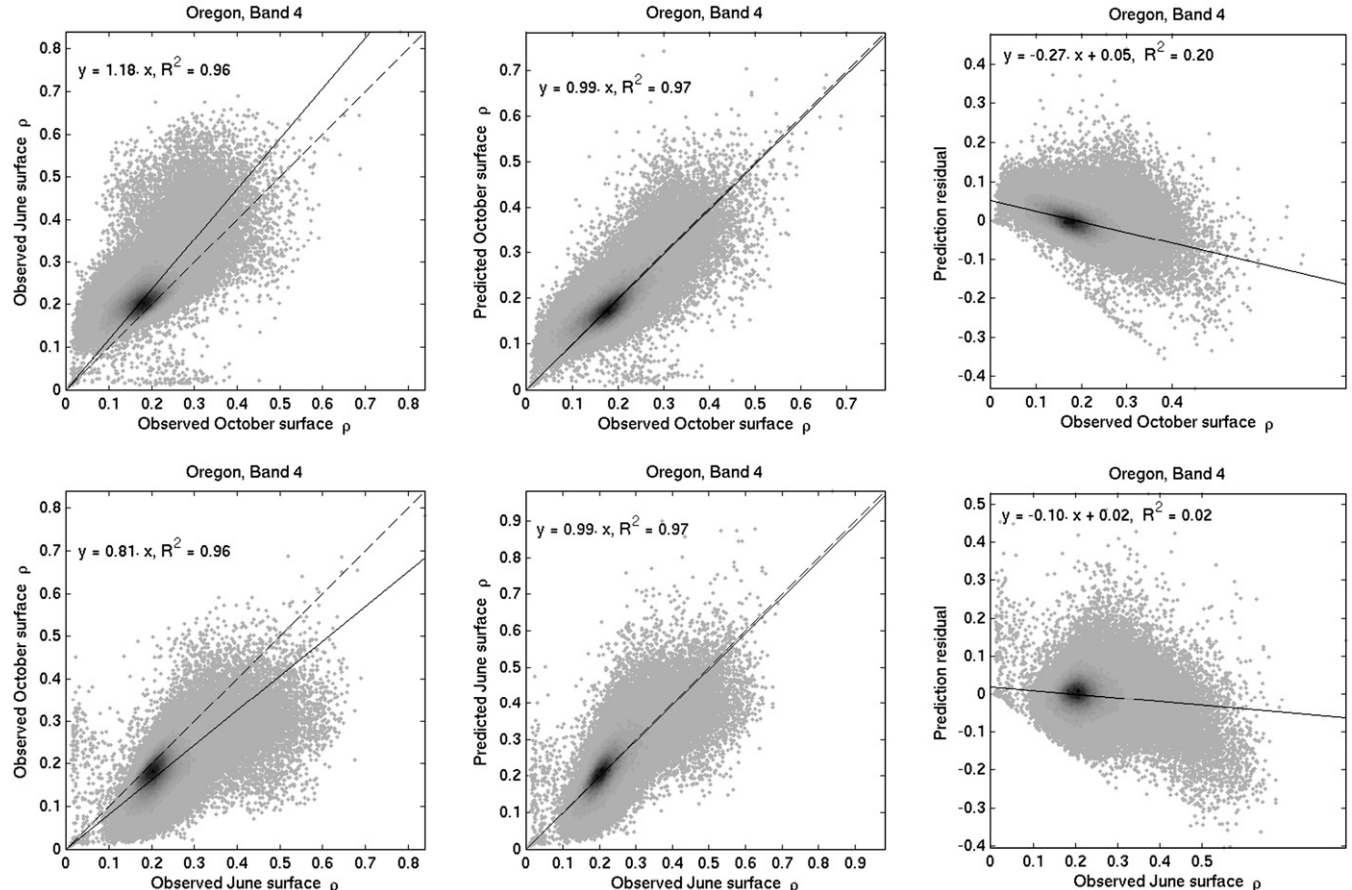


**Fig. 9.** Scatterplots of the Oregon scene 6S corrected near-infrared (band 4) reflectance, showing observed versus predicted reflectance, and prediction residual versus observed reflectance, for the two acquisition dates October 6th 2000 and June 16th 2000. The top row illustrates prediction of October 6th 2000 reflectance, and the bottom row illustrates prediction of June 16th 2000 reflectance. A simple regression line through the origin of these data is shown superimposed (solid line). Because of the large number of 30 m pixels, these data are shown for 30 m pixels sampled regularly every 10 rows and 10 columns from across the image; 362,446 pixels are illustrated. The frequency of occurrence of pixels with the same reflectance is illustrated by density shading with darker tones illustrating higher frequency of occurrence.

temporal residuals (black) — occurring at only 12% of the pixels, primarily located along contrast boundaries and in regions of high spatial reflectance variation occurring at scales smaller than the 500 m MODIS BRDF/Albedo pixel dimension. These locations may in part be due to misregistration and resampling impacts that are greatest in regions of high spatial frequency variation (Roy, 2000), but may also reflect regions of textural change i.e. the Landsat reflectance coefficient of variation within the MODIS pixels was not constant between the two dates due to surface changes.

Tables 4 and 5 summarize the prediction residuals and the temporal residuals computed over the entire study site for predictions in both temporal directions i.e., predicting November 25th ETM+ TOA reflectance (Table 4) and predicting January 9th TOA reflectance (Table 5). These results and the residual standard deviations are illustrated in Fig. 3. The mean prediction residuals are lower than the mean temporal residuals, for all spectral bands and in both temporal directions, implying that the prediction method is on average better than temporal pixel substitution. Generally, the standard deviations of the prediction residuals (vertical line lengths in Fig. 3) are higher in the infrared bands 4, 5, 7 than the visible bands 2, 3, with the exception of band 1. There is no strong spectral pattern among the mean residuals, although the highest residuals occur in ETM+ band 4 (NIR: 0.78–0.90 μm). This in part reflects differences in the spectral properties of the scene components, whereby for example, healthy vegetation has low red reflectance and high near-infrared reflectance. To illustrate this, Fig. 4 shows the mean reflectance normalized residuals (Eq. (7)) summarized in Tables 4 and 5. As before, the prediction residuals are lower than the temporal equivalents. The normalized prediction and temporal residuals are most similar in

ETM+ band 2 (green: 0.53–0.61 μm) and most dissimilar in band 4 (near-infrared: 0.78–0.90 μm), perhaps reflecting the greater impact of atmospheric contamination at shorter wavelengths. The ratios,  $\bar{\Delta}_{\text{prediction}}/\bar{\Delta}_{\text{temporal}} = \Delta_{\text{prediction}}^*/\Delta_{\text{temporal}}^*$ , tabulated in Tables 4 and 5, indicate that the prediction residuals are on average approximately one third the temporal residuals (0.38 and 0.29 in predicting November 25th and January 9th respectively) for band 4, and 0.94 the temporal residuals for band 2.

Figs. 5 and 6 show scatterplots for the two ETM+ bands with the greatest (band 4) and smallest (band 2) difference between the mean reflectance normalized prediction and temporal residuals respectively. The figures show scatterplots of the four possible combinations of observed and predicted reflectance on the two ETM+ acquisition dates (left two columns), and of the prediction residuals (computed as Eq. (5) but not taking the absolute value) plotted against observed reflectance (right column). Each plotted point corresponds to a 30 m pixel; because of the large number of pixels considered, only results for pixels selected systematically every 10 pixels in the image row and columns are shown and a grey scale shading scheme is used to illustrate the frequency of pixels having the same specific x and y axis reflectance values. Linear regression lines forced to pass through the reflectance origin are superimposed to quantify the observed relationships. For the band 4 near-infrared reflectance (Fig. 5), the scatterplots of observed reflectance for the two dates have regression coefficients further from unity (0.75 and 1.31, left column) than the scatterplots of observed against predicted reflectance for the same date (1.01 and 0.98, middle column). In addition, the prediction residual scatterplots (right column) show no significant biases. Evidently, the prediction methodology is working well for the NIR

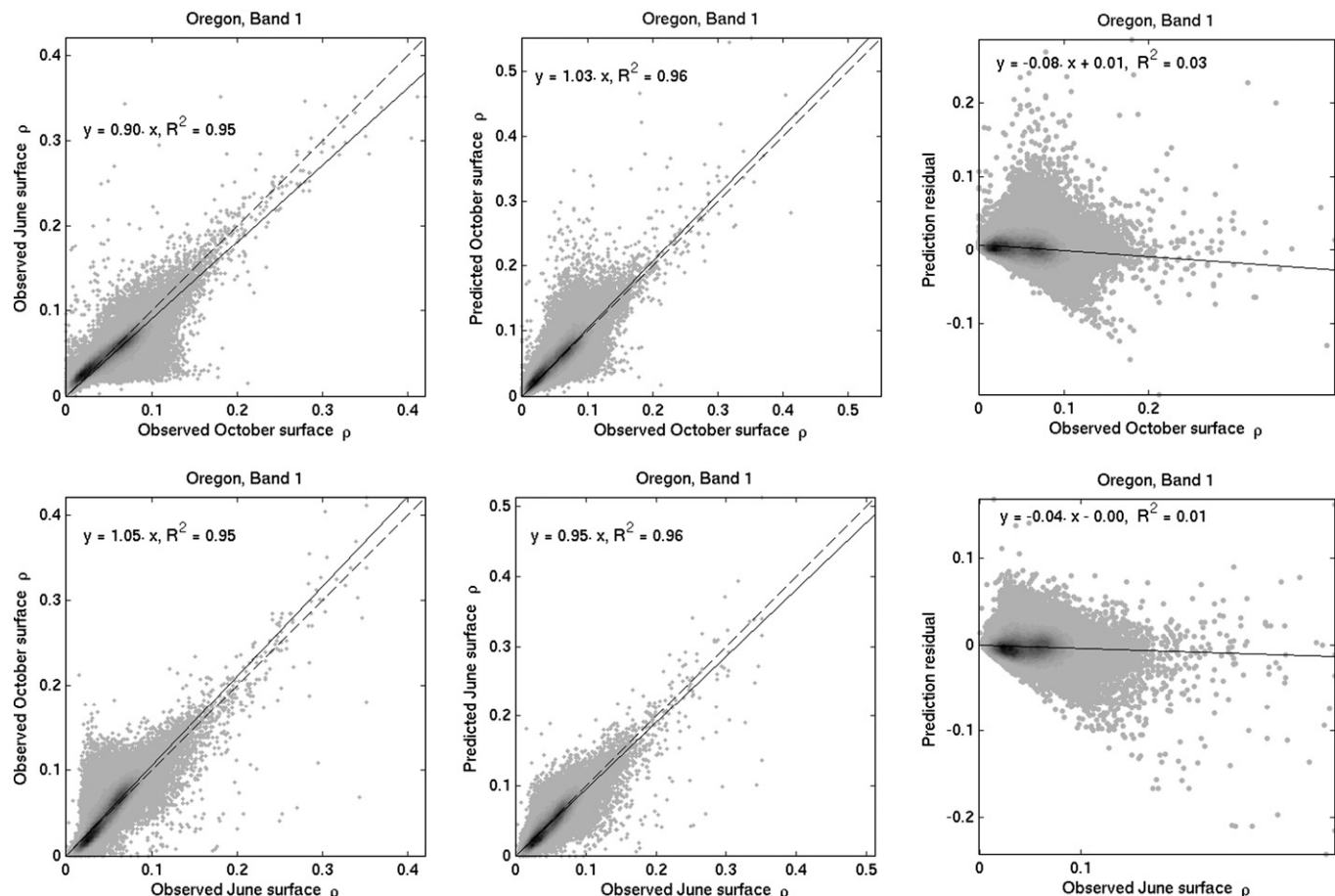


**Fig. 10.** Scatterplots of the Oregon scene 6S corrected blue (band 1) reflectance, showing observed versus predicted reflectance, and prediction residual versus observed reflectance, for the two acquisition dates October 6th, 2000 and June 16th, 2000. See Fig. 9 caption for further details.

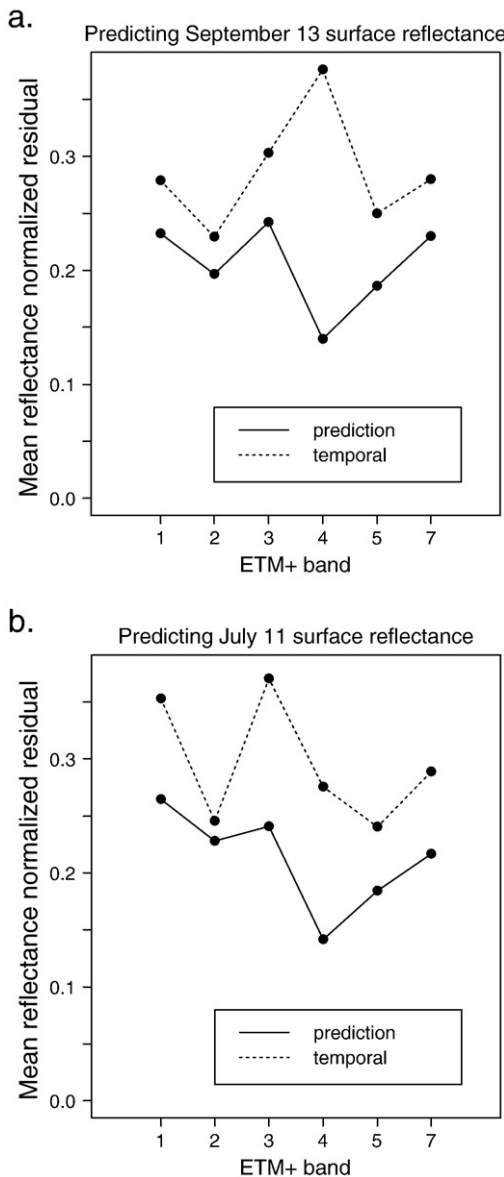


**Fig. 11.** Mean reflectance normalized prediction residuals (solid lines) and temporal residuals (dotted lines) in predicting (a) September 13th 2000 and (b) July 11th 2000 reflectance, for the 6 reflective bands of the 6S corrected Idaho Landsat data.

band for predictions in either direction. Conversely, the scatterplots for the band 2 green reflectance (Fig. 6) show only marginal difference in these respects, although the prediction residual scatterplots (right column) indicate no bias. This may be due to atmospheric contamination at shorter wavelengths; Rayleigh scattering is nearly 5 times as strong in the green band as in the NIR, and aerosol scattering frequently more significant at this shorter wavelength. Evidently, the prediction methodology does not work

as well for more atmospherically contaminated shorter wavelength Landsat data.

### 6.2. Oregon study site results

Figs. 7 and 8 show the mean reflectance normalized residuals for TOA reflectance (i.e. without 6S correction) and for surface reflectance (i.e. with 6S correction) respectively. The median AODs at 0.55 μm for the June 16th and October 6th acquisitions were 0.11 and 0.05 respectively, i.e., not high. The relative spectral impact of the atmospheric correction is clearly evident on the shorter wavelength visible ETM+ bands 1 and 2 – the mean reflectance normalized prediction residuals decrease relative to the temporal residuals when 6S correction is applied. The atmospheric correction makes marginal relative difference to the residual values at longer wavelengths.

The mean reflectance normalized residuals are lower than or equal to the equivalent temporal residuals, for all spectral bands and in both temporal directions, for the 6S corrected data (Tables 6 and 7). As with the Africa results, the normalized prediction and temporal residuals are most dissimilar in ETM+ band 4 (near-infrared: 0.78–0.90 μm) with  $\bar{\Delta}_{\text{prediction}}/\bar{\Delta}_{\text{temporal}} = \Delta_{\text{prediction}}^*/\Delta_{\text{temporal}}^*$  ratios 0.52 and 0.64 for the two prediction directions, but are most similar in the shortest wavelength ETM+ band 1 (blue: 0.45–0.52 μm) with  $\bar{\Delta}_{\text{prediction}}/\bar{\Delta}_{\text{temporal}} = \Delta_{\text{prediction}}^*/\Delta_{\text{temporal}}^*$  ratios of 1.00 and 0.89 (Tables 6 and 7).

Figs. 9 and 10 illustrate scatterplots of the same nature as those shown previously for the African site, for the two 6S corrected ETM+ bands with the greatest (band 4) and smallest (band 1) difference between the mean reflectance normalized prediction and temporal residuals respectively. Similar results for band 4 NIR reflectance are observed (Fig. 9) as for Africa – the scatterplots of observed reflectance for the two dates (left column) have regression coefficients further from unity (1.18 and 0.81) and lower  $R^2$  values than the scatterplots of observed against predicted reflectance for the same date (middle column). In addition, the prediction residual scatterplots (right column) show no significant biases. The scatterplots of observed band 1 blue reflectance for the two dates (Fig. 10) have regression coefficients similar to the scatterplots of observed against predicted reflectance for the same dates and comparable  $R^2$  values, and no significant biases in the prediction residual scatterplots (right column).

### 6.3. Idaho study site results

The median AODs for the Idaho acquisitions were similar to those for Oregon (0.11 and 0.04 AOD at 0.55 μm for the Idaho July 11th and September 13th acquisitions respectively). Fig. 11 shows the mean reflectance normalized residuals for the Idaho 6S corrected surface reflectance data. These results are summarized in Tables 8 and 9. Similar results to Oregon and Africa are observed, with the mean reflectance normalized residuals lower than the equivalent temporal residuals, for all spectral bands and in both temporal directions. The largest difference between the prediction and temporal residuals occurs in band 4 (near-infrared: 0.78–0.90 μm) with  $\bar{\Delta}_{\text{prediction}}/\bar{\Delta}_{\text{temporal}} = \Delta_{\text{prediction}}^*/\Delta_{\text{temporal}}^*$  ratios 0.37 and 0.51 for the two prediction directions, and the least for band 2 (green: 0.53–0.61 μm) which has ratios of 0.86 and 0.93.

**Table 8**  
Idaho study site summary statistics: predicting September 13th 2000 ETM+ 6S corrected surface reflectance using July 11th 2000 ETM+ 6S corrected surface reflectance data and contemporaneous MODIS products (Tables 2 and 3)

	Band 1	Band 2	Band 3	Band 4	Band 5	Band 7
$\bar{\Delta}_{\text{temporal}}$	0.012	0.014	0.020	0.070	0.043	0.028
$\Delta_{\text{temporal}}^*$	0.279	0.230	0.303	0.376	0.250	0.280
$\bar{\Delta}_{\text{prediction}}$	0.010	0.012	0.016	0.026	0.032	0.023
$\Delta_{\text{prediction}}^*$	0.233	0.197	0.242	0.140	0.186	0.230
$\bar{\Delta}_{\text{prediction}}/\bar{\Delta}_{\text{temporal}} = \Delta_{\text{prediction}}^*/\Delta_{\text{temporal}}^*$	0.83	0.86	0.80	0.37	0.74	0.82
2000/09/13 mean surface reflectance	0.043	0.061	0.066	0.186	0.172	0.100

**Table 9**

Idaho study site summary statistics: predicting July 11th 2000 ETM+ 6S corrected surface reflectance using September 13th 2000 ETM+ 6S corrected surface reflectance data and contemporaneous MODIS products (Tables 2 and 3)

	Band 1	Band 2	Band 3	Band 4	Band 5	Band 7
$\bar{\Delta}_{\text{temporal}}$	0.012	0.014	0.020	0.070	0.043	0.028
$\Delta_{\text{temporal}}$	0.353	0.246	0.370	0.276	0.240	0.289
$\bar{\Delta}_{\text{prediction}}$	0.009	0.013	0.013	0.036	0.033	0.021
$\Delta_{\text{prediction}}^*$	0.265	0.228	0.241	0.142	0.184	0.216
$\bar{\Delta}_{\text{prediction}}/\bar{\Delta}_{\text{temporal}} = \Delta_{\text{prediction}}^*/\Delta_{\text{temporal}}^*$	0.75	0.93	0.65	0.51	0.77	0.75
2000/07/11 mean surface reflectance	0.034	0.057	0.054	0.254	0.179	0.097

#### 6.4. Significant temporal change

Fig. 12 illustrates for two 10 km × 10 km spatial subsets of the U.S. Idaho scene, how the method handles significant temporal reflectance changes, due primarily to relief shadow and solar illumination changes (top) and due to agricultural harvesting (bottom). Significant reflectance changes of this nature are difficult to accommodate using conventional relative radiometric normalization and gap filling techniques. For each subset, the ETM+ NIR 6S corrected reflectance observed on July 11th and September 13th 2000 and the predicted September 13th NIR reflectance are shown along with the prediction and temporal residuals and the locations where the prediction residuals are greater than the temporal residuals.

The first subset (Fig. 12, top two rows) is of a mountainous area with evident topographic relief variation. In the observed July ETM+ subset (Fig. 12a1) the solar zenith angle is 29.9° whereas in the observed September ETM+ image (Fig. 12a2) the solar zenith angle is 45.9° and substantial relief shadow and differential illumination effects caused by spatial changes in the orientation of the surface (Teillet et al., 1982) are apparent. The MODIS BRDF/Albedo product does not explicitly consider terrain slope and aspect effects and so their impacts are to some degree included in the MODIS BRDF spectral model parameters. The predicted September 13th reflectance (Fig. 12a3) captures the broad spatial distribution of the relief shadow occurring at the 500 m MODIS scale. In general, the temporal residuals (Fig. 12a4) are higher than the prediction residuals (Fig. 12a5). The mean temporal residual and mean prediction residual for this subset are 0.053 and 0.029 respectively, corresponding to 35% and 19% of the mean observed NIR September 13th reflectance (0.152). The prediction residuals are greater than the temporal residuals for 32% of the pixels, primarily on sun-facing slopes (Fig. 12a6). Their location may be due to the bias in derived surface reflectance which does not account for topographic local variations in the solar zenith angle, and because of uncertainties in the Landsat view and solar illumination vectors, as no terrain correction was applied.

The second subset (Fig. 12, bottom two rows) is of an agricultural area containing many fields of approximately 800 m × 800 m dimension. The observed July surface ETM+ NIR reflectance (Fig. 12b1) is higher than the observed September surface reflectance (Fig. 12b2) with many fields harvested by the later acquisition date. Despite the evident land cover change complexity, the predicted September 13th reflectance captures many of the temporal changes (Fig. 12b3). The mean temporal residual and mean prediction residual for this subset are 0.130 and 0.044 respectively, corresponding to 56% and 19% of the mean observed September 13th NIR reflectance (0.231). The prediction residuals are greater than the temporal residuals for only 13% of the pixels in the subset (Fig. 12b6), primarily at fields with a higher NIR reflectance in September than in July, and along high contrast edges.

Close examination of the predicted reflectance for the two subsets (Fig. 12a3 and b3) reveals a faint blocky pattern that corresponds spatially to the locations of the resampled 500 m MODIS pixel dimensions. This pattern is most evident across some of the fields (Fig. 12b3). If the BRDF dynamics are different between one field and its neighbor (e.g., due to harvesting in one field and not in an

adjacent field), then a MODIS correction value (modulation term  $c$  in Eq. (4)) that lies partially in both fields cannot adequately compensate for this. This is consistent with the observations made in Section 2 that the assumptions underlying the method are less likely to be valid where the Landsat reflectance heterogeneity at the sub-MODIS pixel scale changes temporally. To investigate this further, Fig. 13 shows scatterplots of the coefficient of variation of the 30 m Landsat reflectances for the entire Idaho scene and for the two 10 km × 10 km spatial subsets. Each plotted point corresponds to the coefficient of variation of the observed NIR reflectance falling in a MODIS 500 m pixel for the July and September Landsat acquisition dates. The coefficient of variation values for the entire scene (Fig. 13a) shows a reasonable overall correspondence between the two dates ( $R^2=0.53$ ), i.e. the coefficient of variation is somewhat constant even though this scene contains areas of extensive land cover change. Conversely, and as expected, the  $R^2$  values for the subsets are lower (0.47, topographic variation subset and 0.18, agricultural harvesting subset), reflecting less reliable performance of the fusion method where the sub-MODIS pixel scale reflectance heterogeneity changes temporally.

#### 6.5. MODIS BRDF model parameter quality

The accuracy of the prediction (Eq. (4)) is dependent upon the noise in the observed Landsat ETM+ data, the accuracy of the Landsat solar illumination and viewing geometry characterization, and the accuracy of the predicted MODIS reflectance. All of these factors vary in space and time. The accuracy of the predicted MODIS reflectance (Eq. (1)) is dependent on the degree of noise and the angular sampling of the 16 days of MODIS surface reflectance observations used to invert the BRDF model (Lucht & Lewis, 2000; Schaaf et al., 2002). Previous researchers have modeled the MODIS BRDF predicted reflectance error as the product of the root mean square of the residuals of the BRDF inversion (used as an estimate of noise in the observations and the lack of ability of the model to fit the measurements), and an angularly dependent weight of determination (Lucht & Lewis, 2000; Roy et al., 2002). As discussed in Section 3.2 this information is quantified in the MODIS BRDF/Albedo quality product (MCD43A2) as five values coded 0–4 indicating decreasing inversion quality. Table 10 summarizes the MCD43A2 information for the two dates used to undertake the predictions. To reduce the complexity of this analysis, the 5 quality levels are aggregated to two levels – full inversion (better quality) and magnitude inversion (poor quality), and as before, only ETM+ pixels with valid inversions are considered. For any prediction (Eq. (4)) there are four possible date-quality combinations as two MODIS dates were used. Thus, Table 10 summarizes the percentages of the ETM+ pixels with these date-quality combinations in each ETM+ band at each site, and the corresponding mean prediction and mean temporal residuals computed over the pixels with these four date-quality combinations. The number of pixels considered (second column of Table 10) varies spectrally because the availability of valid MODIS MCD43 pixels changes among bands, due to bad detectors in certain bands and because at shorter wavelengths MODIS observations sensed under high aerosol conditions are not used (Lucht et al., 2000).

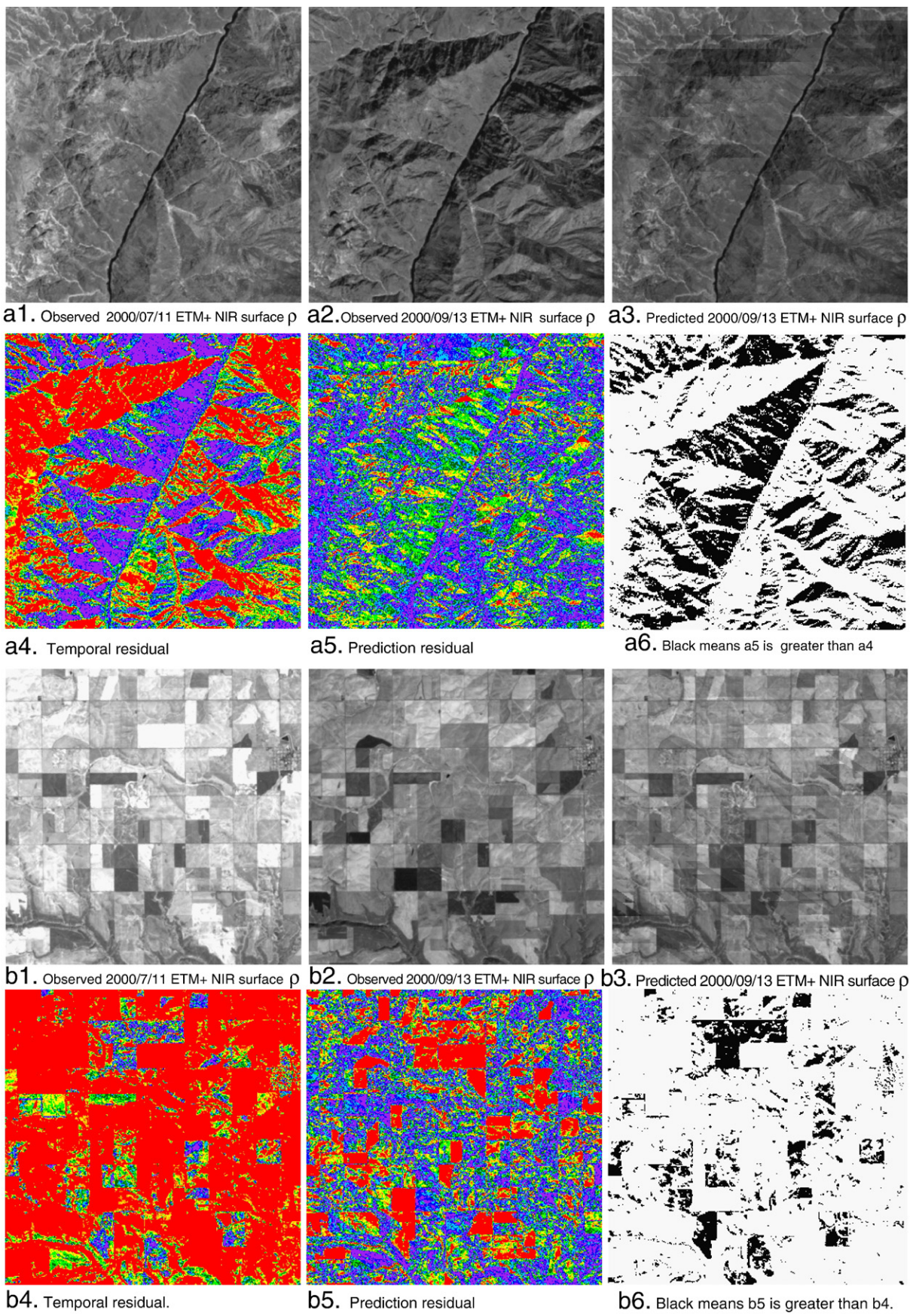


**Fig. 12.** Two 10 km × 10 km subsets of the Idaho scene illustrating the spatially explicit residuals in predicting near-infrared September 13th Landsat surface reflectance from July 11th surface reflectance and MODIS surface reflectance modeled for both dates ETM+ geometry; a1–a6 are for a mountainous area and b1–b6 are for an agricultural area. The same contrast stretch is applied to the spectral images in each row but not between rows. The residuals values are color coded as in Fig. 2:  $0 \leq \text{purple} < 0.015$ ,  $0.015 \leq \text{blue} < 0.03$ ,  $0.03 \leq \text{green} < 0.045$ ,  $0.045 \leq \text{yellow} < 0.06$ ,  $0.06 \leq \text{orange} < 0.09$ ,  $\text{red} \geq 0.09$ .

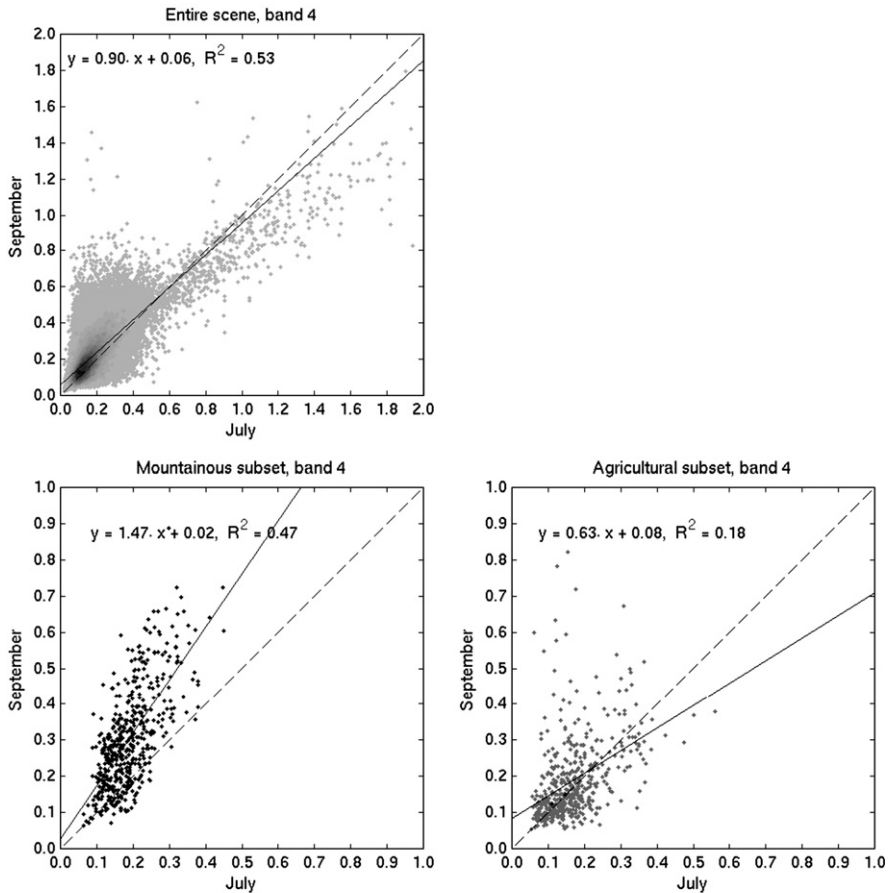


**Fig. 13.** Scatterplots of the coefficient of variation of 30 m Landsat NIR reflectance within corresponding 500 m MODIS pixels for July 11th 2000 and September 13th 2000 Landsat acquisitions for (a) the entire Idaho scene, (b) the mountainous 10 km × 10 km spatial subset shown in the top two rows of Fig. 12, (c) the agricultural 10 km × 10 km spatial subset shown in the bottom two rows of Fig. 12. In (a) 157,618 MODIS pixels are illustrated while in (b) and (c) only 494 MODIS pixels are illustrated.

For the African site 16%–30% of the pixels have MODIS BRDF model parameters derived from full inversions and 28–45% from magnitude inversions on both dates. The quality of the prediction is always poorer if only magnitude inversion data are available for both dates. For cases where full inversion data are available for only one date, the quality of the prediction generally lies between these two. This pattern is expected and corroborates the validity of the MODIS BRDF model parameter quality product. For the Oregon and Idaho sites, between 92% and 97% of the ETM+ pixels have corresponding BRDF parameters derived from two full inversions while less than 1% of the pixels have corresponding BRDF parameters derived from two magnitude inversions, reflecting the effect of different cloud climatology in tropical Africa and temperature North America on the MODIS BRDF model parameter retrieval. The pattern of the prediction quality for the US sites is similar to the Africa site, although not as clear, perhaps due to the small sample size of the poor quality inversions. These results suggest that the MODIS BRDF parameter quality product (MCD43A2) should be incorporated in any characterization of prediction uncertainty from this method.

## 7. Discussion and conclusions

This paper has presented a semi-physical fusion approach that uses the MODIS BRDF/Albedo product and existing Landsat observations to predict Landsat reflectance for any viewing or solar illumination angles. Consequently, Landsat reflectance may be predicted on the same, an antecedent, or subsequent Landsat acquisition date, in a way that is appropriate for pixel level gap filling applications,

such as Landsat SLC-off processing and cloud/cloud shadow filling, and for relative radiometric normalization. The method is most accurate for the ETM+ near-infrared (NIR) band, with mean NIR prediction residuals of 9%, 12% and 14% of the mean NIR scene reflectance of the predicted dates for the African, Oregon and Idaho Landsat test scenes respectively. Prediction results are generally better for the infrared bands than for the visible bands, most likely due to the greater influence of atmospheric effects at shorter wavelengths. The error in Landsat reflectance prediction is generally much less than that assuming no change between observations; mean prediction residuals computed across the Landsat scenes are 0.38–0.83 (red band) and 0.29–0.64 (NIR band) of the mean temporal residuals.

The major strengths of the method are that it is simple to implement and that it requires no scene-dependent tuning, meaning global application should be possible, and, importantly, it accommodates for temporal variations due to surface changes (e.g., phenological, land cover/land use variations) observable at the 500 m MODIS BRDF/Albedo product resolution. The method does however require adequate data co-registration, computation of Landsat satellite viewing and solar geometry, and Landsat cloud and cloud shadow detection, and ideally Landsat atmospheric correction, which are still not insignificant issues for operational implementation. The method is applicable to any high spatial resolution satellite data, provided the wavelengths considered, specifically the spectral response functions (Teillet et al., 2007), are similar to those available from the MODIS instruments; further research work is required to quantify the impact of spectral filter response differences.

**Table 10**

The mean prediction residual compared to the mean temporal residual with respect to the quality of the MODIS BRDF model parameters of the two dates for the three sites

a. Africa						
	# of pixels considered	% of pixels with different QA states	Predicting 2001/11/25		Predicting 2001/01/09	
Band 1	28,944,620	16%	27%	0.013/0.024=0.55	0.011/0.023=0.45	0.021/0.024=0.88
		12%	45%	0.014/0.025=0.58	0.017/0.024=0.69	0.023/0.025=0.92
Band 2	29,184,569	26%	25%	0.012/0.017=0.73	0.019/0.016=1.21	0.012/0.017=0.74
		13%	36%	0.014/0.017=0.79	0.017/0.017=1.02	0.014/0.017=0.80
Band 3	29,089,348	24%	27%	0.007/0.028=0.27	0.009/0.024=0.38	0.010/0.028=0.38
		12%	37%	0.008/0.027=0.29	0.010/0.021=0.45	0.011/0.027=0.39
Band 4	29,435,069	30%	28%	0.025/0.067=0.36	0.025/0.067=0.37	0.018/0.067=0.26
		14%	28%	0.025/0.063=0.39	0.023/0.056=0.41	0.019/0.063=0.29
Band 5	29,412,983	30%	27%	0.016/0.024=0.67	0.015/0.017=0.86	0.018/0.024=0.73
		14%	29%	0.016/0.023=0.70	0.013/0.014=0.92	0.017/0.023=0.75
Band 7	29,303,203	29%	27%	0.011/0.031=0.36	0.009/0.022=0.43	0.015/0.031=0.50
		13%	31%	0.011/0.027=0.41	0.008/0.012=0.71	0.015/0.027=0.55
b. Oregon						
	# of pixels considered	% of pixels with different QA states	Predicting 2000/10/06		Predicting 2000/06/16	
Band 1	36,243,948	93%	1%	0.009/0.009=1.00	0.011/0.014=0.81	0.008/0.009=0.89
		6%	11,579	0.008/0.008=0.96	0.019/0.024=0.80	0.007/0.008=0.90
Band 2	36,244,905	94%	1%	0.010/0.013=0.78	0.016/0.023=0.69	0.011/0.013=0.82
		5%	890	0.008/0.013=0.66	0.027/0.040=0.67	0.010/0.013=0.79
Band 3	36,244,186	94%	1%	0.015/0.018=0.86	0.023/0.031=0.73	0.013/0.018=0.75
		5%	4821	0.024/0.060=0.40	0.056/0.098=0.57	0.011/0.014=0.81
Band 4	36,246,801	96%	1%	0.022/0.042=0.52	0.032/0.050=0.65	0.027/0.042=0.64
		3%	711	0.024/0.060=0.40	0.056/0.098=0.57	0.033/0.060=0.55
Band 5	36,246,345	96%	1%	0.035/0.044=0.79	0.044/0.055=0.79	0.037/0.044=0.84
		3%	478	0.034/0.045=0.75	0.069/0.078=0.89	0.037/0.045=0.82
Band 7	36,244,898	95%	1%	0.028/0.031=0.92	0.036/0.039=0.91	0.028/0.031=0.91
		4%	2888	0.025/0.029=0.86	0.065/0.055=1.17	0.025/0.029=0.87
c. Idaho						
	# of pixels considered	% of pixels with different QA states	Predicting 2000/09/13		Predicting 2000/07/11	
Band 1	36,919,817	92%	7%	0.010/0.012=0.87	0.010/0.011=0.91	0.009/0.012=0.79
		1%	66,219	0.007/0.007=1.04	0.006/0.006=1.13	0.007/0.007=1.09
Band 2	36,920,057	94%	5%	0.012/0.014=0.89	0.012/0.013=0.93	0.013/0.014=0.92
		1%	41,733	0.007/0.008=0.94	0.006/0.005=1.12	0.009/0.008=1.15
Band 3	36,920,057	92%	6%	0.016/0.020=0.81	0.014/0.018=0.77	0.013/0.020=0.64
		1%	48,735	0.008/0.008=1.01	0.006/0.006=1.08	0.008/0.008=1.02
Band 4	36,920,057	97%	2%	0.026/0.070=0.38	0.033/0.084=0.39	0.036/0.070=0.52
		156,059	4516	0.027/0.049=0.55	0.027/0.042=0.65	0.032/0.049=0.65
Band 5	36,920,057	96%	5%	0.032/0.042=0.75	0.035/0.051=0.68	0.033/0.042=0.78
		1%	19,913	0.027/0.034=0.80	0.025/0.032=0.77	0.030/0.034=0.88
Band 7	36,920,057	94%	5%	0.023/0.028=0.82	0.020/0.028=0.73	0.021/0.028=0.77
		1%	42,179	0.016/0.020=0.78	0.012/0.017=0.69	0.018/0.020=0.91

In column 3 of the main table, "% of pixels with different QA states", the four percentages in each cell refer to the percentage of ETM+ pixels that have the corresponding MODIS BRDF model parameter Quality Assessment (QA) states for the two dates  $t_1$  and  $t_2$  conforming to:

		$t_2$
$t_1$	Full inversion	%
	Magnitude inversion	%

in which  $t_1$  and  $t_2$  refer to the earlier and later of the two dates respectively for each site; when the percentage is less than 1% the actual number of pixels is shown. The last two columns of the main table summarize the ratios of the mean prediction residual (numerator) to the mean temporal residual (denominator) for the pixels with the corresponding QA states in column 3. Note that the ratio is computed before the nominator and denominator are rounded to 3 decimal places and therefore there may be equations like  $0.016/0.016=1.04$ .

Issues revealed by the prototyping are associated primarily with the scale discrepancy between the 500 m MODIS BRDF/Albedo product and the 30 m ETM+ data. This discrepancy is most apparent when the reflectance changes in a spatially heterogeneous manner at scales larger than the 30 m Landsat pixels and smaller than the 500 m MODIS pixels, for example, where 500 m MODIS pixels are not aligned with changing patterns in the 30 m Landsat data, such as field boundaries with different field temporal dynamics. This scale discrepancy cannot be easily mitigated without using a higher spatial resolution MODIS modulation factor (Eq. (4)), derived for example from the MODIS 250 m red and near-infrared bands. If the bulk BRDF effects over a Landsat scene are relatively constant then it may be appropriate to spatially smooth the MODIS modulation factor prior to application, although this would smooth high spatial frequency effects of land cover dynamics, such as those occurring at field boundaries. The impact of topographic influences (relief shadow and differential illumination) was also observed to be an issue, but improvements may be obtained by using Landsat Level 1T data (terrain corrected) data in conjunction with digital elevation model data. Note also that the impact of snow has not been investigated in this study but that the MODIS BRDF/Albedo product only captures snow events that persist within each 16 day period and so may not reflect the impact of ephemeral snowcover. Further research is required in all these respects.

Further work is ongoing to assess the suitability of the method for quantitative remote sensing applications. If the results of the method are to be used in any quantitative sense, it is important to attempt to define an uncertainty with each prediction. The methods given by Lucht and Lewis (2000) allow for a prediction of uncertainty due to angular interpolation/extrapolation and may be combined with radiometric and atmospheric correction uncertainty estimates (Roy et al., 2002). Such information is used in the derivation of the BRDF/Albedo product Quality Assessment (QA) flags, although this is not available in a full description to the user of the final product. Analysis of the MCD43 QA states however lends some weight to using this quantized QA information as an input to uncertainty estimates, although further work is required to accurately quantify a mapping between the QA flags and uncertainty in reflectance.

The method may be applied to normalize BRDF influences to simulate any desired viewing or illumination angles. In particular, it may be useful for normalizing Landsat reflectance to nadir viewing geometry (view zenith 0°), as well as correcting for effects due to variations in solar zenith angle and differences due to temporal dynamics. In this way, if Landsat data were available at low cost then they could be normalized to generate seamless large area temporal composite mosaic products, providing a high spatial resolution analogue to the moderate and coarse spatial resolution products generated from the MODIS and AVHRR data streams (Justice et al., 2002; Tucker et al., 2005). In addition to science applications, Landsat data have had a large impact through their use as background imagery in virtual globe tools such as Google Earth and NASA World Wind (Boschetti et al., in press; Butler 2006). An enhancement to such tools could potentially be achieved by using these mosaics to provide a visualization of the landscape as a function of time as well as space.

A next generation of operational moderate spatial resolution global polar-orbiting remote sensing systems is planned for the NPOESS Preparatory Project (NPP) and the National Polar Orbiting Environmental Satellite System (NPOESS), to be launched in 2010 and in the following decade respectively, and a similar BRDF/Albedo algorithm is scheduled for implementation. The high spatial resolution Landsat Data Continuity Mission (LDCM) is planned for launch in 2011. This schedule emphasizes the need for early prototyping of polar-orbiting data fusion for large scale land surface studies. The capabilities demonstrated in this paper for integrating MODIS and Landsat ETM+ data show potential for NPP/NPOESS-LDCM data fusion.

## Acknowledgements

Mike J. Choate, contractor to U.S. Geological Survey (USGS) Center for Earth Resources Observation, is thanked for his time and effort in generating the Landsat view and solar geometry data. Dr. P. Lewis was partially supported by the UK NERC through the Centre for Terrestrial Carbon Dynamics (CTCD). This work was partially funded by NASA grants NNG04GP09G, NNG04HZ18C, and NNG04HZ72C.

## References

- Ackerman, S. A., Strabala, K. I., Menzel, W. P., Frey, R. A., Moeller, C. C., & Gumley, L. E. (1998). Discriminating clear sky from clouds with MODIS. *Journal of Geophysical Research*, 103, 32141–32157.
- Arvidson, T., Gasch, J., & Goward, S. N. (2001). Landsat 7's long-term acquisition plan – An innovative approach to building a global imagery archive. *Remote Sensing of Environment*, 78, 13–26.
- Asner, G. P., & Warner, A. S. (2003). Canopy shadow in IKONOS satellite observations of tropical forests and savannas. *Remote Sensing of Environment*, 87(4), 521–533.
- Breiman, L. (1996). Bagging predictors. *Machine Learning*, 26, 123–140.
- Boschetti, L., Roy, D. P., & Justice, C. O. (in press). Using NASA's World Wind Virtual Globe for interactive internet visualisation of the Global MODIS Burned Area Product. *International Journal of Remote Sensing*.
- Butler, D. (2006). The web-wide world. *Nature*, 439, 776–778.
- Chander, G., Markham, B. L., & Barsi, J. A. (2007). Revised Landsat-5 Thematic Mapper radiometric calibration. *IEEE Geoscience and Remote Sensing Letters*, 4(3), 490–494.
- Chavez, P. S., Jr. (1996). Image-based atmospheric corrections – Revisited and improved. *Photogrammetric Engineering and Remote Sensing*, 62(9), 1025–1036.
- Coppin, P., Jonckheere, I., Nackaerts, K., Muys, B., & Lambin, E. (2004). Digital change detection methods in ecosystem monitoring: A review. *International Journal of Remote Sensing*, 25, 1565–1596.
- Danaher, T., Wu, X., & Campbell, N. (2001). Bi-directional reflectance distribution function approaches to radiometric calibration of Landsat TM imagery. *Proceedings of the IEEE Geoscience and Remote Sensing Symposium (IGARSS 2001)*, 6, 2654–2657.
- d'Entremont, R. P., Schaaf, C. B., Lucht, W., & Strahler, A. H. (1999). Retrieval of red spectral albedo and bidirectional reflectance from 1-km<sup>2</sup> satellite observations for the New England region. *Journal of Geophysical Research*, 104, 6229–6339.
- Friedl, M. A., McIver, D. K., Hodges, J. C. F., Zhang, X. Y., Muchoney, D., Strahler, A. H., et al. (2002). Global land cover mapping from MODIS: Algorithms and early results. *Remote Sensing of Environment*, 83, 288–303.
- Gao, F., Jin, Y., Xiaowen, L., Schaaf, C. B., & Strahler, A. H. (2002). Bidirectional NDVI and atmospherically resistant BRDF inversion for vegetation canopy. *IEEE Transactions on Geoscience and Remote Sensing*, 40, 1269–1278.
- Gao, F., Masek, J., Hall, J., & Schwaller, M. (2006). On the blending of the Landsat and MODIS surface reflectance: Predicting daily Landsat surface reflectance. *IEEE Transactions on Geoscience and Remote Sensing*, 44(8), 2207–2218.
- Gao, F., Schaaf, C., Strahler, A. H., & Lucht, W. (2001). Using a multi-kernel least variance approach to retrieve and evaluate albedo from limited BRDF observations. *Remote Sensing of Environment*, 76, 57–66.
- Goward, S. N., Masek, J. G., Williams, D. L., Irons, J. R., & Thompson, R. J. (2001). The Landsat 7 mission, terrestrial research and applications for the 21st century. *Remote Sensing of Environment*, 78, 3–12.
- Hansen, M. C., Roy, D. P., Lindquist, E., Justice, C. O., & Altstaat, A. (2008). A method for integrating MODIS and Landsat data for systematic monitoring of forest cover and change in Central Africa. *Remote Sensing of Environment*, 112, 2495–2513.
- Helder, D. L., & Ruggles, T. A. (2004). Landsat thematic mapper reflective-band radiometric artifacts. *IEEE Transactions on Geoscience and Remote Sensing*, 42(12), 490–494.
- Helmer, E. H., & Ruefenacht, B. (2005). Cloud-free satellite image mosaics with regression trees and histogram matching. *Photogrammetric Engineering and Remote Sensing*, 71, 1079–1089.
- Huete, A. R., Didan, K., Miura, T., Rodriguez, E. P., Gao, X., & Ferreira, L. G. (2002). Overview of the radiometric and biophysical performance of the MODIS vegetation indices. *Remote Sensing of Environment*, 83, 195–213.
- Irish, R. I., Barker, J. L., Goward, S. N., & Arvidson, T. (2006). Characterization of the Landsat-7 ETM+ automated cloud-cover assessment (ACCA) algorithm. *Photogrammetric Engineering & Remote Sensing*, 72(10), 1179–1188.
- Irons, J. R., & Masek, J. G. (2006). Requirements for a Landsat Data Continuity Mission. *Photogrammetric Engineering and Remote Sensing*, 72(10), 1102–1108.
- Jin, Y., Schaaf, C., Gao, F., Li, X., Strahler, A., Bruegge, C., et al. (2002). Improving MODIS surface BRDF/Albedo retrieval with MISR multi-angle observations. *IEEE Transactions on Geoscience and Remote Sensing*, 40, 1593–1604.
- Jin, Y., Schaaf, C. B., Woodcock, C. E., Gao, F., Li, X., Strahler, A. H., et al. (2003). Consistency of MODIS surface BRDF/Albedo retrievals: 1. Algorithm performance. *Journal of Geophysical Research*, 108(D5), 4158. doi:10.1029/2002JD002803
- Jin, Y., Schaaf, C. B., Woodcock, C. E., Gao, F., Li, X., Strahler, A. H., et al. (2003). Consistency of MODIS surface BRDF/Albedo retrievals: 2. Validation. *Journal of Geophysical Research*, 108(D5), 4159. doi:10.1029/2002JD002804
- Ju, J., & Roy, D. P. (2008). The availability of cloud-free Landsat ETM+ data over the conterminous United States and globally. *Remote Sensing of Environment*, 112, 1196–1211.
- Justice, C., Townshend, J., Vermote, E., Masuoka, E., Wolfe, R., Saleous, N., et al. (2002). An overview of MODIS Land data processing and product status. *Remote Sensing of Environment*, 83, 3–15.

- Kaufman, Y. J. (1987). The effect of subpixel clouds on remote sensing. *International Journal of Remote Sensing*, 8, 839–857.
- Kaufman, Y. J., Wald, A., Remer, L. A., Gao, B., Li, R., & Flynn, L. (1997). The MODIS 2.1 mm channel – correlation with visible reflectance for use in remote sensing of aerosol. *IEEE Transactions on Geoscience and Remote Sensing*, 35, 1286–1298.
- Kotchenova, S., Vermote, E., Matarrese, R., & Klemm, F., Jr. (2006). Validation of a vector version of the 6S radiative transfer code for atmospheric correction of satellite data. Part I: Path radiance. *Applied Optics*, 45, 6762–6774.
- Lambin, E. F. (1999). Monitoring forest degradation in tropical regions by remote sensing: Some methodological issues. *Global Ecology and Biogeography*, 8, 191–198.
- Lacaze, R., & Roujean, J. L. (2001). G-function and HOt Spot (GHOST) reflectance model—Application to multi-scale airborne POLDER measurements. *Remote Sensing of Environment*, 76, 67–80.
- Lee, D. S., Storey, J. C., Choate, M. J., & Hayes, R. (2004). Four years of Landsat-7 on-orbit geometric calibration and performance. *IEEE Transactions on Geoscience and Remote Sensing*, 42, 2786–2795.
- Liang, S., Fang, H., & Chen, M. (2001). Atmospheric correction of Landsat ETM+ land surface imagery. I. Methods. *IEEE Transactions on Geoscience and Remote Sensing*, 39 (11), 2490–2498. doi:10.1109/36.964986
- Liang, S., Fang, H., Morisette, J. T., Chen, M., Shuey, C. J., Walthall, C. L., et al. (2002). Atmospheric correction of Landsat ETM+ land surface imagery: II. Validation and applications. *IEEE Transactions on Geoscience and Remote Sensing*, 40(12), 2736–2746.
- Lucht, W., & Lewis, P. (2000). Theoretical noise sensitivity of BRDF and albedo retrieval from the EOS-MODIS and MISR sensors with respect to angular sampling. *International Journal of Remote Sensing*, 21(1), 81–89.
- Lucht, W., Schaaf, C. B., & Strahler, A. H. (2000). An algorithm for the retrieval of albedo from space using semiempirical BRDF models. *IEEE Transactions on Geoscience and Remote Sensing*, 38, 977–998.
- Masek, J. G., Vermote, E. F., Saleous, N. E., Wolfe, R., Hall, F. G., Huemmrich, K. F., et al. (2006). A Landsat surface reflectance dataset for North America, 1990–2000. *IEEE Transactions on Geoscience and Remote Sensing Letters*, 3(1), 68–72.
- Maxwell, S. K., Schmidt, G. L., & Storey, J. C. (2007). A multi-scale segmentation approach to filling gaps in Landsat ETM+ SLC-off images. *International Journal of Remote Sensing*, 28(23), 5339–5356.
- Moody, E. G., King, M. D., Platnick, S., Schaaf, C. B., & Gao, F. (2005). Spatially complete global spectral surface albedos: Value-added datasets derived from Terra MODIS land products. *IEEE Transactions on Geoscience and Remote Sensing*, 43, 144–158.
- Olfhof, I., Pouliot, D., Fernandes, R., & Latifovic, R. (2005). Landsat-7 ETM+ radiometric normalization comparison for northern mapping applications. *Remote Sensing of Environment*, 95, 388–398.
- Ouaidrari, H., & Vermote, E. F. (1999). Operational atmospheric correction of Landsat TM data. *Remote Sensing of Environment*, 70, 4–15.
- Pinty, B., Taberner, M., Liang, S., Govaerts, Y., Martonchik, J. V., Lattanzio, A., et al. (2004). Intercomparison of surface albedo products from various spaceborne sensors. *Proceedings of the Workshop on Inter-Comparison of Large Scale Optical and Infrared Sensors, ESA ESTEC, Noordwijk, The Netherlands, 12–14 October 2004. ESA ESTEC*.
- Platnick, S., King, M. D., Ackerman, S. A., Menzel, W. P., Baum, B. A., Riédi, J. C., et al. (2003). The MODIS cloud products: Algorithms and examples from Terra. *IEEE Transactions on Geoscience and Remote Sensing*, 41, 459–473.
- Pohl, C., & Van Genderen, J. L. (1998). Multisensor image fusion in remote sensing: Concepts, methods and applications. *International Journal of Remote Sensing*, 19(5), 823–854. doi:10.1080/014311698215748
- Privette, J. L., Eck, T. F., & Deering, D. W. (1997). Estimating spectral albedo and nadir reflectance through inversion of simple BRDF models with AVHRR/MODIS-like data. *Journal of Geophysical Research*, 102, 29,529–29,542.
- Quaife, T., Lewis, P., De Kauwe, M., Williams, M., Law, B., Disney, M. I., et al. (2008). Assimilating canopy reflectance data into an ecosystem model with an ensemble Kalman filter. *Remote Sensing of Environment*, 112, 1347–1364.
- Roy, D. P. (2000). The impact of misregistration upon composited wide field of view satellite data and implications for change detection. *IEEE Transactions on Geoscience and Remote Sensing*, 38, 2017–2032.
- Roy, D. P., & Dikshit, O. (1994). Investigation of image resampling effects upon the textural information content of a high spatial resolution remotely sensed image. *International Journal of Remote Sensing*, 15, 1123–1130.
- Roy, D. P., & Singh, S. (1994). The importance of instrument pointing accuracy for surface bidirectional reflectance distribution mapping. *International Journal of Remote Sensing*, 15, 1091–1099.
- Roy, D. P., Lewis, P., & Justice, C. (2002). Burned area mapping using multi-temporal moderate spatial resolution data — a bi-directional reflectance model-based expectation approach. *Remote Sensing of Environment*, 83, 263–286.
- Roy, D. P., Lewis, P., Schaaf, C., Devadiga, S., & Boschetti, L. (2006). The Global impact of cloud on the production of MODIS bi-directional reflectance model based composites for terrestrial monitoring. *IEEE Geoscience and Remote Sensing Letters*, 3, 452–456.
- Roujean, J.-L., Leroy, M., & Deschamps, P. Y. (1992). A bi-directional reflectance model of the Earth's surface for the correction of remote sensing data. *Journal of Geophysical Research*, 97, 20255–20468.
- Salomon, J., Schaaf, C. B., Strahler, A. H., Gao, F., & Jin, Y. (2006). Validation of the MODIS bidirectional reflectance distribution function and albedo retrievals using combined observations from the aqua and terra platforms. *IEEE Transactions on Geoscience and Remote Sensing*, 44(6), 1555–1565.
- Schaaf, C., Gao, F., Strahler, A., Lucht, W., Li, X., Tsang, T., et al. (2002). First operational BRDF, albedo and nadir reflectance products from MODIS. *Remote Sensing of Environment*, 83, 135–148.
- Schott, J. R., Salvaggio, C., & Volchock, W. K. (1988). Radiometric scene normalization using pseudo-invariant features. *Remote Sensing of Environment*, 26, 1–16.
- Song, C., & Woodcock, C. E. (2003). Monitoring forest succession with multitemporal Landsat images: Factors of uncertainty. *IEEE Transactions on Geoscience and Remote Sensing*, 41(11), 2557–2567.
- Standish, E. M., Newhall, X. X., Williams, J. G., & Yeomans, D. K. (1992). Orbital ephemerides of the sun, moon and planets. In P. K. Seidelmann (Ed.), *Explanatory supplement to the astronomical almanac* (pp. 279–374). Mill Valley, CA: University Books.
- Storey, J., Scaramuzza, P., & Schmidt, G. (2005). Landsat 7 scan line corrector-off gap filled product development. *Pecora 16 Conference Proceedings*, 23–27 October 2005, Sioux Falls, South Dakota.
- Strugnell, N., & Lucht, W. (2001). An algorithm to infer continental-scale albedo from AVHRR data, land cover class and field observations of typical BRDFs. *Journal of Climate*, 14, 1360–1376.
- Strugnell, N., Lucht, W., & Schaaf, C. (2001). A global albedo data set derived from AVHRR data for use in climate simulations. *Geophysical Research Letters*, 28, 191–194.
- Teillet, P. M., Fedosejevs, G., Thome, K. J., & Barker, J. L. (2007). Impacts of spectral band difference effects on radiometric cross-calibration between satellite sensors in the solar-reflective spectral domain. *Remote Sensing of Environment*, 110, 393–409.
- Teillet, P. M., Guindon, B., & Goodenough, D. G. (1982). On the slope-aspect correction of multispectral scanner data. *Canadian Journal of Remote Sensing*, 8(2), 1537–1540.
- Toivonen, T., Kalliari, R., Ruokolainen, K., & Malik, R. N. (2006). Across-path DN gradient in Landsat TM imagery of Amazonian forests: A challenge for image interpretation and mosaicing. *Remote Sensing of Environment*, 100, 550–562.
- Tucker, C. J., Pinzon, J. E., Brown, M. E., Slayback, D. A., Pak, E. W., Mahoney, R., et al. (2005). An extended AVHRR 8-km NDVI data set compatible with MODIS and SPOT vegetation NDVI data. *International Journal of Remote Sensing*, 26(20), 4485–4498.
- van Leeuwen, W. J. D., Orr, B. J., Marsh, S. E., & Herrmann, S. M. (2006). Multi-sensor NDVI data continuity: Uncertainties and implications for vegetation monitoring applications. *Remote Sensing of Environment*, 100, 67–81.
- Vermote, E. F., & Roy, D. P. (2002). Land surface hot-spot observed by MODIS over Central Africa. *International Journal of Remote Sensing*, 23, 2141–2143 cover and letter.
- Vermote, E. F., El Saleous, N., & Justice, C. (2002). Atmospheric correction of the MODIS data in the visible to middle infrared: First results. *Remote Sensing of Environment*, 83(1–2), 97–111.
- Wanner, W., Strahler, A. H., Hu, B., Lewis, P., Muller, J.-P., Li, X., et al. (1997). Global retrieval of bidirectional reflectance and albedo over land from EOS MODIS and MISR data: Theory and algorithm. *Journal of Geophysical Research*, 102, 17,143–17,162.
- Williams, D. L., Goward, S., & Arvidson, T. (2006). Landsat: Yesterday, today, and tomorrow. *Photogrammetric Engineering & Remote Sensing*, 72(10), 1171–1178.
- Wolfe, R., Nishihama, M., Fleig, A., Kuypers, J., Roy, D., Storey, J., et al. (2002). Achieving sub-pixel geolocation accuracy in support of MODIS land science. *Remote Sensing of Environment*, 83, 31–49.
- Wolfe, R., Roy, D., & Vermote, E. (1998). The MODIS land data storage, gridding and compositing methodology: L2 Grid. *IEEE Transactions on Geoscience and Remote Sensing*, 36, 1324–1338.
- WWW1. The Landsat 7 ETM+ Geometric Algorithm Theoretical Basis Document. [http://landsathandbook.gsfc.nasa.gov/handbook/pdfs/L7\\_geometry\\_ATBD.pdf](http://landsathandbook.gsfc.nasa.gov/handbook/pdfs/L7_geometry_ATBD.pdf)
- WWW2. The MODIS Level 1A Earth Location: Algorithm Theoretical Basis Document Version 3.0. [http://modis.gsfc.nasa.gov/data/atbd/atbd\\_mod28\\_v3.pdf](http://modis.gsfc.nasa.gov/data/atbd/atbd_mod28_v3.pdf)
- WWW3. The MODIS Reprojection Tool. [http://edcdaac.usgs.gov/landdaac/tools/modis\\_index.asp](http://edcdaac.usgs.gov/landdaac/tools/modis_index.asp)